CRREL REPORT 96-8

Source Location and Tracking Capability of a Small Seismic Array

Mark L. Moran and Donald G. Albert

June 1996

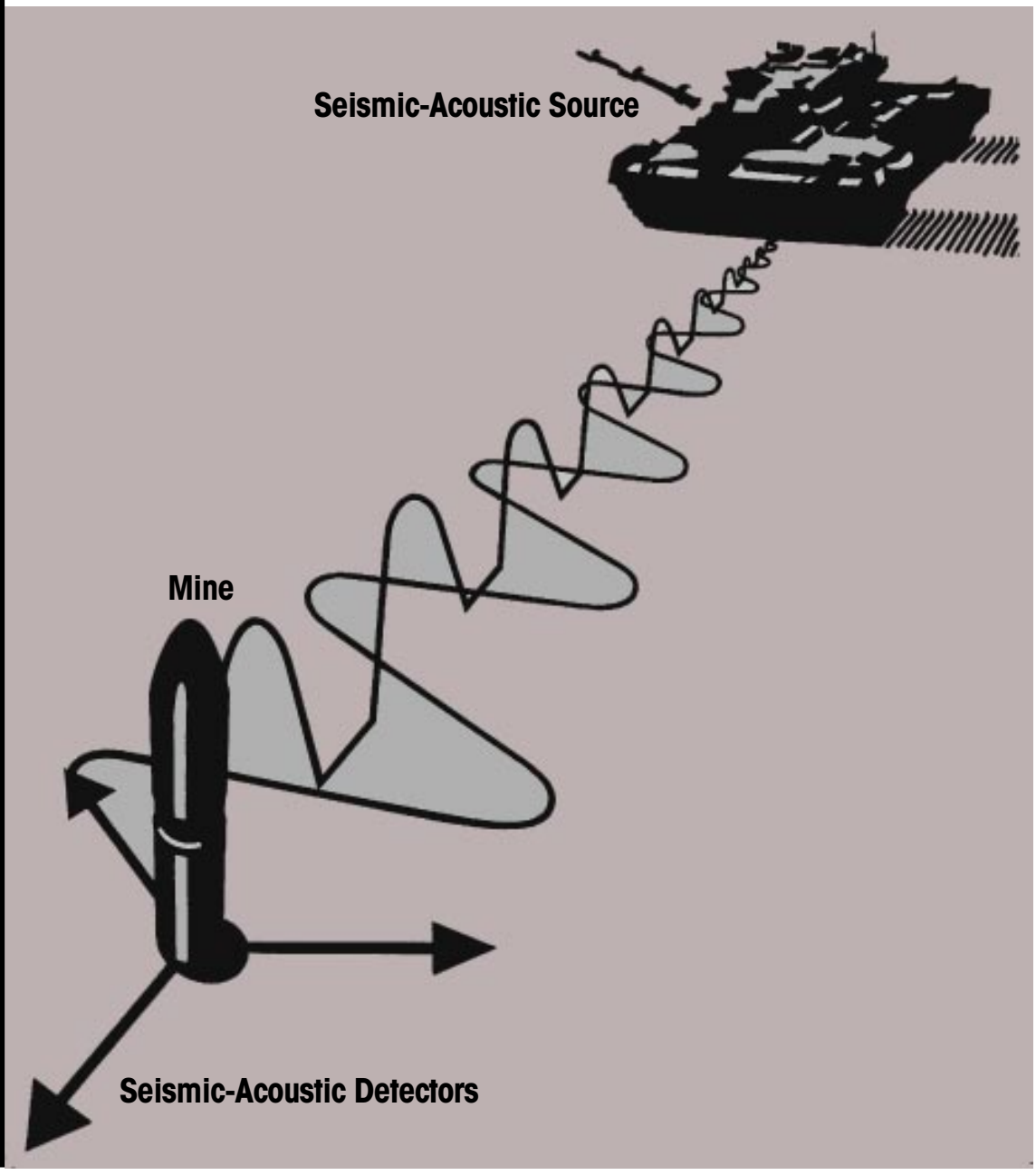

Abstract: Recordings of seismic wavefields from various sources were obtained using a small array of vertical-component geophones under winter conditions at Grayling, Michigan. These data were processed using a frequency-wavenumber domain Capon minimum variance beamformer to estimate the bearing angle and propagation velocity of the waves emitted from the source. The cross power matrix was adaptively estimated using a tapered block-averaging procedure. The wave sources were sledgehammer blows on the ground surface, .45 caliber blank pistol shots, and an M60 tank moving at 4.5 m s^{-1} along a road near the array. Reliable wavenumber spectra were obtained for all sources. Processing results for the hammer blows show that the dominant seismic arrival is a Rayleigh wave traveling at roughly 220 m s^{-1}. For the pistol shots, two arrivals corresponding to the airwave (338 m s^{-1}) and the air-coupled Rayleigh waves (220 m s^{-1}) were observed. The results for these sources were relatively insensitive to the processing parameters used. For the moving vehicle, the dominant signals observed were Rayleigh waves (220 m s^{-1}). Accurate locations were obtained for this moving source, although the processing parameters had to be carefully selected, and the choice of frequency parameters affected the accuracy of the wavenumber results. Maximizing the number of degrees of freedom and the coherence of the frequency estimates and minimizing the variation of the coherence across adjacent frequency bins provided the most consistently reliable strategy for obtaining accurate wavenumber estimates for the moving vehicle. The sensitivity of the wavenumber estimates to the frequency processing parameters seems to be related to the bias in the phase spectra of the signals and will potentially occur in any bearing estimation method that uses temporal frequncy phase spectra.

Cover: Seismic and acoustic arrivals from a moving tank at an intelligent mine sensor array.

How to get copies of CRREL technical publications:

Department of Defense personnel and contractors may order reports through the Defense Technical Information Center:

DTIC-BR SUITE 0944
8725 JOHN J KINGMAN RD
FT BELVOIR VA 22060-6218
Telephone 1 800 225 3842
E-mail help@dtic.mil
msorders@dtic.mil
WWW http://www.dtic.dla.mil/

All others may order reports through the National Technical Information Service:

NTIS
5285 PORT ROYAL RD
SPRINGFIELD VA 22161
Telephone 1 703 487 4650
1 703 487 4639 (TDD for the hearing-impaired)
E-mail orders@ntis.fedworld.gov
WWW http://www.fedworld.gov/ntis/ntishome.html

A complete list of all CRREL technical publications is available from:

USACRREL (CECRL-TL)
72 LYME RD
HANOVER NH 03755-1290
Telephone 1 603 646 4338
E-mail techpubs@crrel.usace.army.mil

For information on all aspects of the Cold Regions Research and Engineering Laboratory, visit our World Wide Web site: http://www.crrel.usace.army.mil

CRREL Report 96-8

U.S. Army Corps of Engineers
Cold Regions Research & Engineering Laboratory

Source Location and Tracking Capability of a Small Seismic Array

Mark L. Moran and Donald G. Albert

June 1996

Prepared for
OFFICE OF THE CHIEF OF ENGINEERS

Source Location and Tracking Capability of a Small Seismic Array

MARK L. MORAN AND DONALD G. ALBERT

1. INTRODUCTION

Acoustic and seismic sensor array processing has many potential applications of interest to the Army. Recent military conflicts have clearly demonstrated the efficiency of smart weapons systems. A critical element in the effectiveness of many of these systems is their ability to discern and track a target in the presence of background noise. The Wide Area Mine (WAM) being developed by the U.S. Army is heavily dependent upon acoustic and seismic sensor information for bearing determination of targets. Weapon systems such as the WAM are designed to recognize, track, and destroy hostile military vehicles such as armor, mobile artillery, and heavy transport vehicles by deploying small arrays of passive acoustic and/or seismic sensors (microphones and geophones) to monitor local seismic and acoustic wavefields. A cartoon of the detection–attack scenario for the WAM device is shown in Figure 1.

Other important areas where acoustic and seismic array processing may be applied include perimeter defense and intrusion detection. In many instances the effectiveness of line-of-sight systems such as radar, infrared, and motion detection systems are compromised or defeated by local topography, vegetation, and obscuring meteorological conditions. In real-world settings, acoustic and seismic waves readily propagate along bending ray paths and are less affected by vegetation and airborne obscurants. This allows coverage of zones currently outside the detection limits of systems that rely on line-of-sight propagation paths. Acoustic and seismic array-based systems are relatively inexpensive and may be produced and deployed in large numbers, providing a substantial perimeter defense or detection capability.

For small array processing systems to function reliably, it is necessary to be able to estimate accurately the wavefield's temporal frequency phase spectrum, even with limited spatial and temporal wavefield samples. When using wavenumber estimation procedures based on beamforming principles, these data constraints make it difficult to obtain reliable estimates of the spatial correlation matrix, which is critical to the beamformer's performance. The spectral bias and variance are the statistical error parameters that describe the reliability of the resulting estimated frequency and wavenumber spectra. *Bias* is a measure of the energy leakage from adjacent frequency bins that erroneously appears at an incorrect frequency; this phenomenon is termed *leakage* and is caused by the sampling distribution in the time (or space) domain. *Variance* is a measure of the stability in the estimate and is a function of the number and degree of independence between samples available to the estimation process.

Beamforming complications may result from source motion, acoustic-to-seismic coupling, inhomogeneous propagation environments, multiple sources, and low signal-to-noise ratios (SNRs). Given the nature of the moving seismic–acoustic sources being considered and the limited quantity of data available, it is important to recognize the nonideality of the observed signals, so that those properties of the signal that have the highest degree of coherency across the observation array can be exploited fully.

The combined effect of these source-dependent characteristics and the problems arising from sparsely sampled short-duration signal vectors has not been previously demonstrated on the beam response function. In this report we show that beamforming techniques can be reliably applied to these types of signal vectors as long as careful attention is paid to the spectral estimation parameters used in the Fourier transform process. We present a few rough guidelines that produce consistently reliable wavenumber estimates from Capon maximum-likelihood beamformers.

Historically, frequency wavenumber domain (F-K) beamforming analysis has been applied to a variety of problems. In seismology, wavenumber beamformers using geophone arrays are routinely used to determine source parameters for regional and teleseismic events as well as to identify nuclear

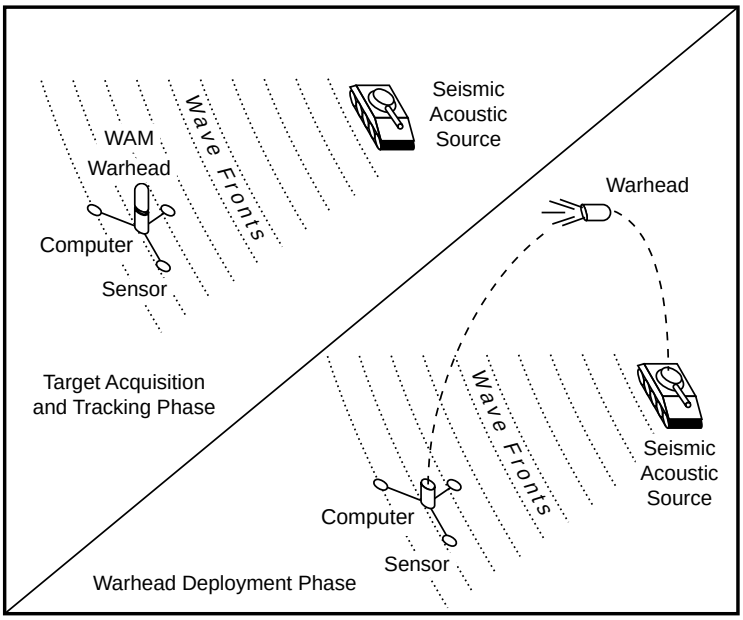

Figure 1. WAM conception of target acquisition and engagement.

explosions. The application of the Capon maximum-likelihood beamformer to teleseismic events using the Large Aperture Seismic Array in Montana was first reported by Capon et al. (1967). In 1969 Capon derived the beamformer and noise suppression characteristics. Beamforming is also applied to sonar problems where passive arrays of hydrophones locate and track submarines and surface vehicles (Hahn 1975). Aircraft tracking with both acoustic and radar technologies and stellar mapping of distant radio-wave emissions are other prominent areas of application for beamforming technology.

The use of seismic and acoustic arrays to track and locate targets of military interest dates from the Vietnam War. Beginning in the late 1960s, military efforts focused, with limited success, on locating artillery positions. In the later 1970s, targets such as surface vehicles were investigated (Cress 1976). Recently, bearing estimation of slow-moving military aircraft using acoustic and seismic array processing technologies has been actively investigated. Of particular note are the efforts of Nawab et al. (1985) and Lacoss et al. (1991), who have successfully tracked both airborne and ground targets at distances of a few kilometers.

Several researchers have investigated the impact of nonideal source attributes on bearing estimates. De Graaf and Johnson (1985) discuss the bias of Bartlett and Capon maximum-likelihood beamformers as a function of SNR under the assumption that the spatial correlation matrix is known exactly and the sources are ideal stationary plane waves. For two or more sources they show that the bias in the wavenumber estimate is a function of the source separation and the degree of coherence between the sources, the SNR, the relative source power, and the number of observation array elements. When the spatial correlation matrix must be estimated from a finite amount of data, De Graaf and Johnson (1985) show how the maximum-likelihood estimator becomes increasingly unstable as the data set is reduced.

Knapp and Carter (1977) and Carter (1977) discussed the impact of source motion on bias in bearing estimation from a two- or three-element array using a time-delay estimation procedure. Gragg (1990) showed that there is a time dependence in the Doppler-shifted spectra observed by a single receiver when an acoustic source has a velocity vector that does not pass through the receiver location. He showed that this time dependence makes the Doppler shift difficult to predict. Unless source motion effects can be corrected, there will be a phase bias in the Fourier estimate of the time series. The impact of the phase bias from source motion on wavenumber estimates remains unquantified.

In the following sections we discuss the beamforming equations and explicitly define the frequency domain estimation process used to gen-

erate the cross-power matrix in the beamforming equations. A confidence interval for the variance in the cross-power matrix is developed. This is followed by a discussion of the experimental setting, data acquisition procedure, and seismic array characteristics. Processing results are then given for an impulsive acoustic source, a pure seismic source, and a moving M60 tank. We obtain accurate wavenumber estimates from the beamformer for all three source types. Next we show that small variations in the parameters used to estimate the cross-power matrix contribute to wavenumber bias effects. These bias effects are summarized for a variety of block lengths, block overlaps, and window types.

2. BEAMFORMING PRINCIPLES

The discussion given here follows Capon (1969) and Johnson (1982). First, a general expression for an F–K beamformer power function is given. The standard Bartlett (BT) and high-resolution Capon maximum-likelihood (ML) beamformer equations are obtained. Following the beamformer derivation, the estimation and conditioning procedures of the spatial correlation matrix are given.

2.1 Beam-power response function

Assume an array of M sensors have vector locations $\vec{R}_m$ in the x–y plane

$$\left(\left| \vec{R}_\mathrm{m} \right| = \sqrt{x_\mathrm{m}^2 + y_\mathrm{m}^2} \right)$$

as shown in Figure 2. Each sensor is a spatial wavefield sample point that records over time. Such a collection of sensor data is termed the signal vector. A wavefield containing a single plane wave source sampled at locations $\vec{R}_\mathrm{m}$ may be represented by a signal vector with components:

$$x_\mathrm{m}(t) = s\left(t + \frac{\vec{R}_\mathrm{m} \bullet \vec{u}_{\mathrm{k_o}}}{c} \right) + n_\mathrm{m}(t) \ , \qquad (1)$$

where $\vec{k}_\mathrm{o}$ is the wavenumber $\left(\left| \vec{k}_\mathrm{o} \right| = 2\pi f / c \right)$, $\vec{u}_{\mathrm{k_o}}$ is the unit vector direction of the source, n_m is the background noise field, and c is the scalar wave propagation velocity. In the frequency domain, eq 1 is

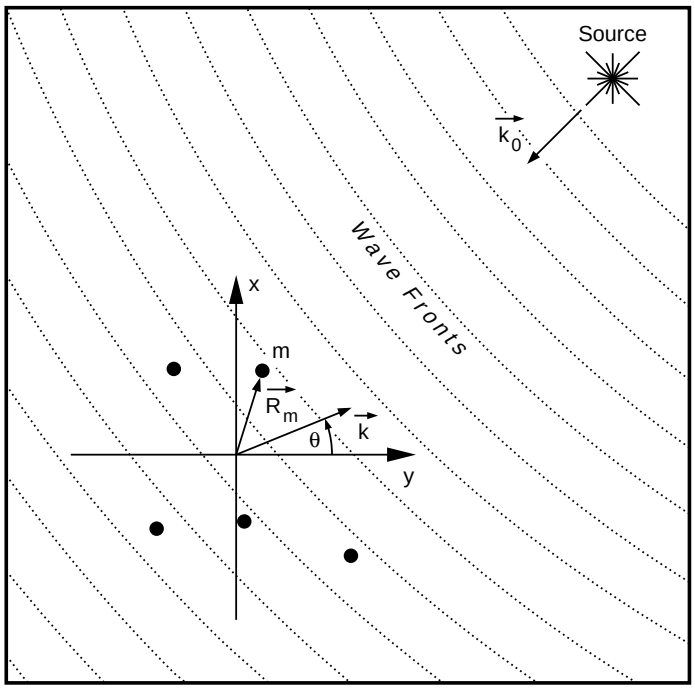

Figure 2. A generic array geometry composed of M *sensors located at vector positions* $\vec{R}_m$. *The pseudo-plane wave source has a wavenumber vector* $\vec{k}_o$. *The observation wavenumber is* $\vec{k}$. *Dots (•) are sensor locations.*

$$X_m(f) = S(f)e^{i\vec{k}_o \bullet \vec{R}_m} + N_m(f), \quad (2)$$

where $S(f)$ is the ideal Fourier transform of the signal without the noise.

In matrix notation, the signal vector is

$$X(f) = \begin{pmatrix} X_0(f) \\ X_1(f) \\ X_2(f) \\ \bullet \\ \bullet \\ \bullet \\ X_{M-1}(f) \end{pmatrix}. \quad (3)$$

Given M spatial samples of the wave field, a beam response function $[Y(f, \vec{k})]$ is formed by summing over each component of the signal vector and applying a phase shift that is dependent upon an observation wavenumber $(\vec{k})$:

$$Y(f, \vec{k}) = \sum_{m=0}^{M-1} a_m e^{-i\vec{k} \bullet \vec{R}_m} X_m(f). \quad (4)$$

Using eq 2 and 4,

$$Y(f, \vec{k}) = \sum_{m=0}^{M-1} a_m(f) \left[S(f) e^{i(\vec{k}_0 - \vec{k}) \bullet \vec{R}_m} + \tilde{N}_m(f) \right] \quad (5)$$

where the $a_m(f)$ constants are spatial filter weights to be defined through the application of a specific beamforming strategy, and $\tilde{N}_m$ is the noise field modified by a phase shift of $e^{i\vec{k} \bullet \vec{R}_m}$. Equation 5 is equivalent to an estimation of the complex wavenumber spectrum of the sampled wavefield. In matrix notation the beam response is

$$Y(f, \vec{k}) = A^{*T} X, \quad (6)$$

where $^*T$ means complex conjugate transpose, and

$$\mathbf{A}(f) = \begin{pmatrix} a_0(f)e^{-i\vec{k} \bullet \vec{R}_0} \\ a_1(f)e^{-i\vec{k} \bullet \vec{R}_1} \\ a_2(f)e^{-i\vec{k} \bullet \vec{R}_2} \\ \bullet \\ \bullet \\ \bullet \\ a_{M-1}(f)e^{-i\vec{k} \bullet \vec{R}_{M-1}} \end{pmatrix} \quad (7)$$

$\mathbf{A}(f)$ is referred to as the steering vector. The beam power at a given frequency and observation wavenumber is

$$P(f, \vec{k}) = \mathbf{A}^{*T} \mathbf{X}\mathbf{X}^{*T} \mathbf{A} \quad (8)$$

or

$$P(f, \vec{k}) = \mathbf{A}^{*T} \mathbf{R}(f) \mathbf{A}, \quad (9)$$

where $\mathbf{R}(f)$ is an $M \times M$ matrix composed of the product of the signal vector and its complex conjugate transpose. The matrix $\mathbf{R}$ is commonly referred to as the spatial correlation matrix. A key result of this report will be to show that subtle changes in the parameters used to estimate the correlation matrix affect the bias in the beam power function.

Equation 9 is the foundation of the wavenumber estimation procedure used in this paper. Referring to eq 5, we see that the maximum of the beam power function occurs when $\vec{k}_0 - \vec{k} = 0$. When performing a narrowband F–K estimation, eq 9 is evaluated at a single frequency over a regularly spaced grid of observation wave-numbers.

A wideband beam power function can be produced by integrating eq 9 over a band of frequencies:

$$P\left(\vec{k}\right) = \int_{f_1}^{f_2} \mathbf{A}^{*T} \mathbf{R} \mathbf{A} df. \quad (10)$$

Recently Nawab et al. (1985) formulated more elegant methods of computing a broadband beamformer.

2.2. Bartlett and Capon maximum-likelihood beamformers

The BT and ML methods are special cases of eq 9 and are a consequence of defining specific values for the $a_m(f)$ weighting functions (eq 5). The BT method is the conventional method of estimating an F–K spectrum. The ML method attempts to minimize energy leakage into the beam response from regions outside the observation wavenumber. This energy leakage problem is the spatial equivalent of frequency domain bias. Thus, $a_m(f)$ is a component of a spatial window function analogous to time series windowing.

If all $a_m(f) = 1$ then eq 9 yields the standard BT beamformer. Under this condition, eq 8 becomes

$$\mathbf{A}' = \begin{pmatrix} e^{-i\vec{k} \bullet \vec{R}_0} \\ e^{-i\vec{k} \bullet \vec{R}_1} \\ e^{-i\vec{k} \bullet \vec{R}_2} \\ \bullet \\ \bullet \\ \bullet \\ e^{-i\vec{k} \bullet \vec{R}_{M-1}} \end{pmatrix}. \quad (11)$$

The power function is

$$\hat{P}_{\mathrm{BT}}\left(f,\vec{k}\right) = \mathbf{A}^{*\mathrm{T}}\hat{\mathbf{R}}\mathbf{A}' , \tag{12}$$

where $\hat{\mathbf{R}}$ is the estimated spatial correlation matrix.

In the ML beamformer, $a_{\mathrm{m}}(f)$ are defined by the properties of the spatial correlation matrix so that spatial energy leakage is minimized. This is done by minimizing the weighted array power function under the constraint that a fixed gain be maintained at the observation wavenumber. Johnson (1982) sets up the problem as

$$\frac{\partial P_{\mathrm{ML}}\left(f,\vec{k}\right)}{\partial \mathbf{W}} = \frac{\partial}{\partial \mathbf{W}}\left(\mathbf{W}^{*\mathrm{T}}\,\mathbf{R}\mathbf{W}\right) = 0 ,$$

$$\text{subject to } \mathbf{W}^{*\mathrm{T}}\,\mathbf{A}' = 1 . \tag{13}$$

$\mathbf{A}'$ is given by eq 11, and $\mathbf{W}$ is defined as the weighted steering vector whose elements are

$$\mathbf{W}_{\mathrm{m}} = a_{\mathrm{m}}\mathbf{A}'_{\mathrm{m}} . \tag{14}$$

The solution to eq 13 is (Johnson 1982, Capon 1969)

$$\mathbf{W} = \frac{\mathbf{R}^{-1}\mathbf{A}'}{\mathbf{A}'^{*\mathrm{T}}\,\mathbf{R}^{-1}\mathbf{A}'} . \tag{15}$$

Note that eq 15 is a function of the spatial correlation matrix. The effect of designing the weighted steering vector using the observed signal properties is that we produce a wavenumber window function that is adaptive to the signal-in-noise field and the specific array geometry. The resultant beampower function is

$$P_{\mathrm{ML}}\left(f,\vec{k}\right) = \mathbf{W}^{*\mathrm{T}}\,\mathbf{R}\mathbf{W} . \tag{16}$$

Substituting eq 15 into 16 and using the estimation for the cross-power matrix, we obtain

$$\hat{P}_{\mathrm{ML}}\left(f,\vec{k}\right) = \frac{1}{\mathbf{A}'^{*\mathrm{T}}\,\hat{\mathbf{R}}^{-1}\mathbf{A}'} , \tag{17}$$

where $\hat{}$ indicates an estimate based on available data.

This is the working form of the ML beamformer used in this paper. It should also be noted that the ML beamformer is also termed a minimum variance method, and in the case of only one coherent signal it is also spatially unbiased (Capon 1969), in the sense that the bias tends toward zero as the number of sensors becomes large. In a multiple-source wavefield the bias is substantially smaller for ML compared with the BT method (De Graaf and Johnson 1985).

2.3. Estimation and conditioning of the correlation matrix

The spatial correlation matrix ($\mathbf{R}$) is constructed from the frequency domain representation of the signal vector $\mathbf{x}$. The properties of the spatial correlation matrix determine the quality of the beampower function. To estimate $\mathbf{R}$ accurately, we use a tapered overlapped block-averaging FFT (OBAFFT). This is a widely utilized procedure for estimating signals with intricate spectra (Welch 1967, Capon et al. 1967). The OBAFFT method allows one to make trade-offs between the bias and variance in the estimate of $\mathbf{R}$.

It is important to guarantee the nonsingularity of the spatial correlation matrix when applying the ML processing procedure. This can be done by the block averaging process or it can be forced by applying a small amount of additive noise to the correlation matrix (Capon 1969). A normalization procedure that produces ones along the diagonal of the spatial correlation matrix is also useful in making qualitative assessments of the accuracy of the wavenumber spectrum.

2.3.1. Tapered overlapped block-averaged FFT

The mathematical procedure used to form the OBAFFT is as follows. The time-domain signal vector obtained from a passive array with M sensors and components such as that of eq 1 has the form

$$\mathbf{x} = \begin{pmatrix} x_0(t) \\ x_1(t) \\ x_2(t) \\ \bullet \\ \bullet \\ \bullet \\ x_{\mathrm{M-1}}(t) \end{pmatrix} . \tag{18}$$

Let $\mathbf{x}$ have N samples at intervals of Δt. Now define a block of this sequence with a length L, such that $L < N$; further, let each block of L samples be overlapped by a percentage p. The number of blocks will be

$$nblks = 1 + \left(\frac{N-L}{nshft}\right), \tag{19}$$

where $nshft = \mathrm{INT}\left[L \times (1-p)\right]$ and INT is the nearest integer operator. Thus, *nblks* gives the total number of overlapped segments (or blocks) that

are overlapped by an integer number of points. The Fourier transform of the *j*th block from channel *m* will be

$$\hat{X}^{j}_{m}(f) = \frac{1}{L}\sum_{\ell=0}^{L-1} a_{\ell} x^{j}_{m}(\ell + j \bullet nshft) e^{-i2\pi f(\ell \Delta t)} \tag{20}$$

where the a_ℓ are time-domain window taper weights. The window tapers decrease the bias in the estimate by ensuring that the ends of each segment of data are gradually tapered to zero.

A variety of window taper functions may be applied, each having a different impact on the properties of the resulting spectral estimate. Harris (1978) presents an excellent overview on window tapering strategies for harmonic analysis problems. Figure 3 graphically illustrates the overlapped (OBAFFT) segmentation.

2.3.2. Formation of spatial correlation matrix

The cross-power function between all pairs of sensors in the array is calculated for each block of data in the OBAFFT method. The final estimate of the spatial correlation matrix is formed by averaging over the block cross-power matrices.

Using eq 20, elements of the cross-power matrix for the *j*th block are

$$R^{j}_{m,n}(f) = X^{j}_{m}(f) * X^{*j}_{n}(f) \ , \tag{21}$$

where *m* and *n* are sensor indices. The final estimate of the spatial correlation matrix is formed by averaging over the block index,

$$R_{m,n}(f) = \frac{1}{nblks}\sum_{j=1}^{nblks} R^{j}_{m,n} \ . \tag{22}$$

The formation of the cross-power function between two vectors produces a vector that has a phase angle that is the difference in phase between the two constituent vectors. For waveforms produced by a stationary source and recorded by channel *m*, the Fourier transform at any given frequency will be a randomly oriented vector. Thus, the OBAFFT gives, for each block of data in channel *m*, a series of vectors with random phase angles. In an array of sensors recording real data, the quantity to be measured is the *phase difference* between channels. The final estimate of the spatial correlation matrix given by eq 22 is therefore an average of several phase angle difference matrices, which becomes less variable as the number of blocks increases. This assumes that the phase difference between channels is not changing with time.

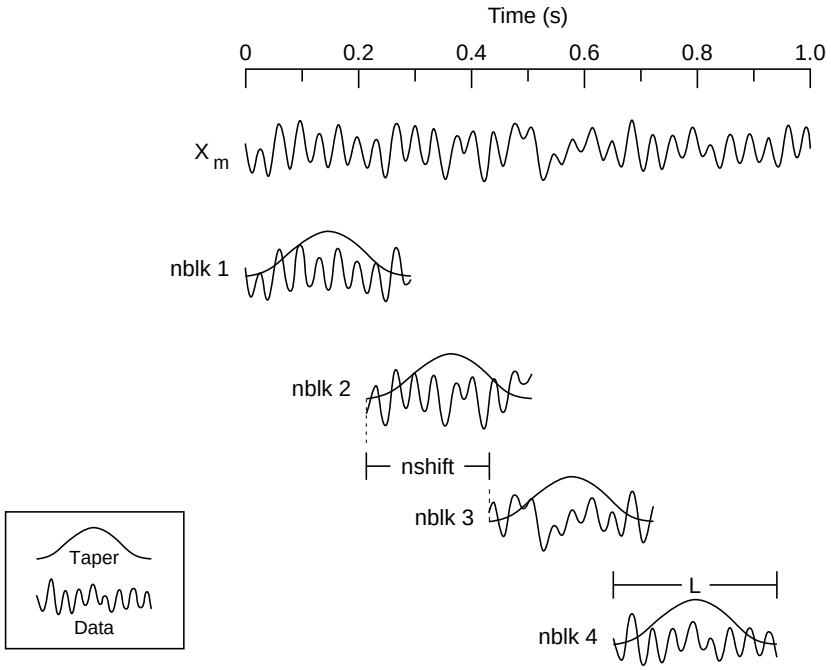

Figure 3. Segmentation and overlapping of a time-domain component of the signal vector. Each tapered block is transformed into the frequency domain via an FFT.

$$\hat{\mathbf{R}}(f) = \begin{pmatrix} \hat{X}_0(f)\hat{X}_0^*(f) & \hat{X}_0(f)\hat{X}_1^*(f) & \hat{X}_0(f)\hat{X}_2^*(f) & \cdots & \hat{X}_0(f)\hat{X}_{M-1}^*(f) \\ \hat{X}_1(f)\hat{X}_0^*(f) & \hat{X}_1(f)\hat{X}_1^*(f) & \hat{X}_1(f)\hat{X}_2^*(f) & \cdots & \hat{X}_1(f)\hat{X}_{M-1}^*(f) \\ \hat{X}_2(f)\hat{X}_0^*(f) & \hat{X}_2(f)\hat{X}_1^*(f) & \hat{X}_2(f)\hat{X}_2^*(f) & \cdots & \hat{X}_2(f)\hat{X}_{M-1}^*(f) \\ \vdots & \vdots & \vdots & \cdots & \vdots \\ \hat{X}_{M-1}(f)\hat{X}_0^*(f) & \hat{X}_{M-1}(f)\hat{X}_1^*(f) & \hat{X}_{M-1}(f)\hat{X}_2^*(f) & \cdots & \hat{X}_{M-1}(f)\hat{X}_{M-1}^*(f) \end{pmatrix} \quad (23)$$

Figure 4. Spatial correlation matrix structure.

2.3.3. Spatial correlation matrix conditioning

The structure of the spatial correlation matrix is given by eq 23 (Fig. 4). In the programmed implementation, each element of this matrix is normalized according to

$$\widehat{\mathbf{R}}_{ij}(f) = \frac{\widehat{\mathbf{X}}_i(f)\widehat{\mathbf{X}}_j^*(f)}{\left|\widehat{\mathbf{X}}_i(f)\right|\left|\widehat{\mathbf{X}}_j(f)\right|} \quad . \quad (24)$$

If the signal vector is perfectly coherent, then the diagonal elements of $\widehat{\mathbf{R}}$ will contain unity values, resulting in a maximum beam power response of 1 when applying the BT method. This allows qualitative judgments to be made on the reliability of the wavenumber estimate, which is particularly important when dealing with nonideal signal types or inhomogeneous propagation environments. When using narrowband BT processing with this normalization, a peak power response < 0.5 is often unreliable.

The existence of the $\widehat{\mathbf{R}}^{-1}$ matrix is of critical importance when applying the ML method (see eq 18). Capon (1969) notes that if the number of blocks (N) in the estimate is less than the number of array sensors (M), then $\widehat{\mathbf{R}}$ is of order M and rank N and is thus singular. This is frequently the case when processing signals of short duration. To guarantee the nonsingularity of the estimated spatial correlation matrix we add a small amount of incoherent noise (λ) to the elements of the spatial correlation matrix. Capon (1969) suggests

$$\widehat{\mathbf{R}}' = (1 - \lambda)\,\widehat{\mathbf{R}} + \lambda \mathbf{I} \, . \quad (25)$$

The choice of λ is determined by trial and error (the results reported here often used values < 10^{-4}). In practice the accuracy of the beam response is relatively insensitive to λ, but it should be kept as small as possible since it lowers the signal-to-noise ratio (SNR) of the beam response.

2.3.4. Variance of the cross-power matrix

The OBAFFT method allows a degree of control over the bias/variance trade-off in the estimate of the cross-power matrix. The bias is mitigated by the choice of window taper and the number of points in each block, while the variance is a function of the number and degree of overlap between blocks. The independence of each block is reduced by increasing the overlap. The characteristics of the window taper applied to each block also affect the block's independence for a given degree of overlap. This partial dependence/independence may be exploited to decrease the variance of a given spectral estimate.

As an illustration of the variance reduction that can be obtained using this strategy, a signal (dt = 1/1023) was generated by superimposing two sine waves with line spectra at 20 and 23 Hz and unitary peak-to-peak amplitudes. The second sine wave series is time-shifted (relative to the first signal) by 0.0455 s (at 20 Hz in the frequency domain this is an approximately 32° phase shift). A unique pseudo-random Gaussian "noise" series with zero mean and a maximum peak-to-peak amplitude of 1 is added to each of the two sine wave signals. This yields an SNR of 1 for each spectral line in the series. The OBAFFT spectral estimation process was applied at 20 Hz for each sine wave plus noise signal, and the cross-power operation was carried out. Note that the presence of the 23-Hz spectral line in the resulting series allows simulation of phase and amplitude bias effects. The 20-Hz OBAFFT estimate of the cross power between the two noisy signals was ob-

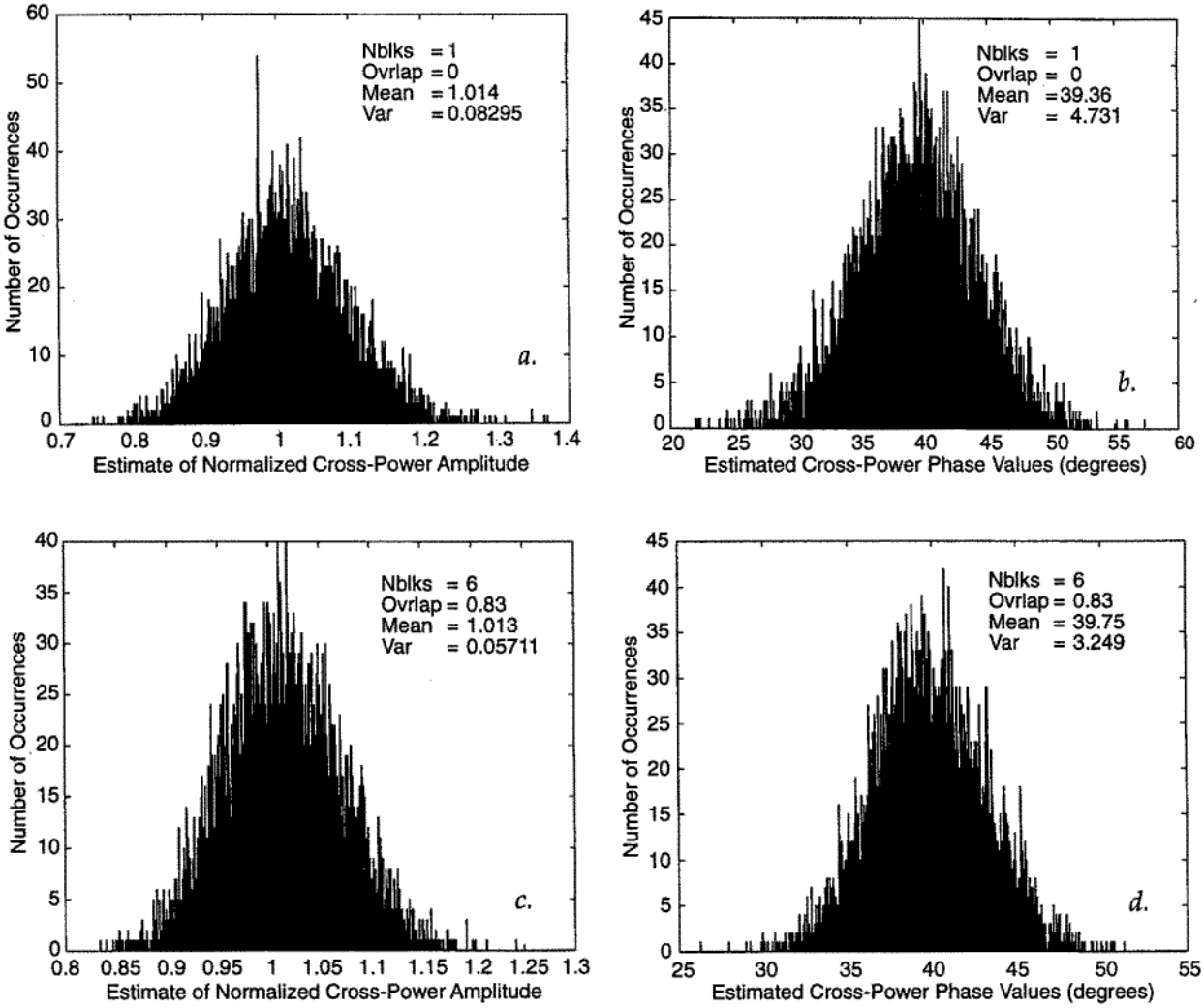

Figure 5. Histograms of cross-power amplitude and phase estimates at 20 Hz for a synthetic sine wave series containing line spectra at 20 and 23 Hz with zero mean random noise. SNR is one. Sample populations for all histograms are composed of 5000 estimates. All estimates utilized a Blackman window taper to reduce bias effects from 23 Hz spectral line. Cross-power histograms shown in (a) and (b) are based on estimates from blocks of 1024 data points. Each estimate in the amplitude and phase histograms shown in (c) and (d) are based on six overlapped blocks of 512 points each. The total series length is 1024 points, and each block overlaps the preceding block by 80%. Note that the variance in histograms (c) and (d) is significantly smaller than the variance seen in (a) and (b).

tained for 5000 different random noise cases. Using this sample population of cross-power values, the mean and variance of the amplitude and phase population can be estimated.

Figure 5 shows cross-power amplitude and phase estimate histograms using the Blackman window function (given by $W(l) = 0.42 - 0.5 \cos\left(\frac{2/\pi}{L-1}\right) + 0.08 \cos\left(\frac{4/\pi}{L-1}\right)$ with $l = 1, \ldots L$). Figure 5a and 5b are the amplitude and phase histograms for the case of estimates based on a single block of 1024 points tapered with a Blackman window function. There are two degrees of freedom in this cross-power estimate. Based on a sample population of 5000 estimates, the amplitude mean is 1.014 with a variance of 0.0829. The phase mean is 39.36 ° with a variance of 4.731°2. In Figure 5c and 5d the amplitude and phase histograms are calculated but the series is estimated using blocks overlapped by 80%. Thus, six partially independent blocks are used in each amplitude and phase estimate. Again using a population of 5000 estimates, the histogram shown in Figure 5c gives an amplitude mean

of 1.013 with a variance of 0.05711. In Figure 5d the phase estimate population yields a mean of 39.75° with a variance of 3.249°2. The critical point to note is the decrease in the variance for the case of the overlapped six block estimates as compared with the variance calculated for the single block estimates. Thus, it is statistically advantageous to use OBAFFT to increase the stability of and decrease the bias in spectral estimation.

2.4. Verification of signal-processing algorithm

The Fortran code implementing the beamforming procedures given above is discussed in detail by Moran (1991). The algorithm was extensively tested during development and continues to be refined. Two tests were used to validate the procedure. The first test was numerical, using a wide variety of synthetic signals under various signal-to-noise ratios (SNRs) and with a variety of frequency bands and array geometries. The second and most critical test came from results obtained from field data collected under defined experimental conditions. These field data tests are based on the impulsive sources discussed in section 5.2.

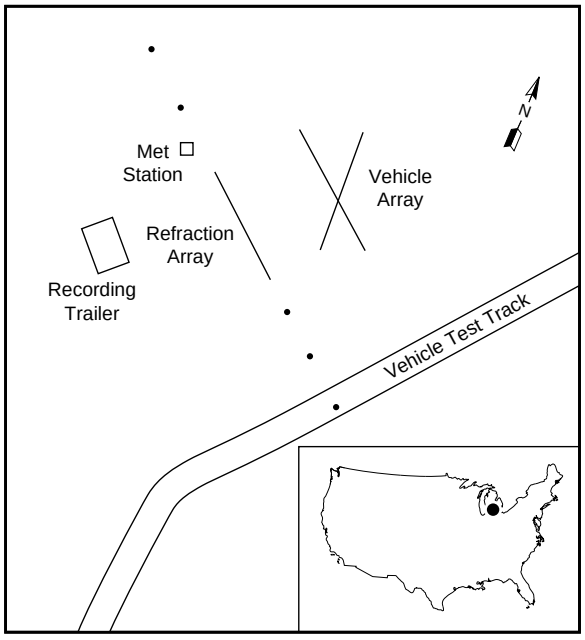

Figure 6. Location map for the seismic experiments, showing vehicle test track, location of contractor's sensors, and location of CRREL seismic arrays. Also shown is the location of the snow pits, met station, frost tubes, and borehole.

3. FIELD DATA ACQUISITION AND EXPERIMENTAL CONDITIONS

To test the efficacy of beamforming, experimental measurements of various sources were obtained. The environmental characteristics of the test site and the methods used to make these recordings are discussed in this section.

3.1. Geological setting

The field tests were performed in February 1988 at Range 37 at the Michigan National Guard's Camp Grayling (Fig. 6). The soil in the Grayling locale consists of glacial outwash sand and gravel (Farrland and Bell 1982). Logs from four wells in the vicinity show the thickness of these deposits at 116, 137, 175, and 251 m, with the bedrock below being Mississippian in age (Lilienthal 1978). A local driller estimated the sand thickness in the area to be around 180 m based on his experience. A borehole 30 m deep was drilled at the site; the soils logged during the drilling are given in Table 1. The characteristics of eight soil samples that were collected off the drill auger are listed in Table 2. These observations show that the site was underlain by medium sand, with some thin layers of fine gravel and clay at depths around 4 and 24 m. The water table was 5.8 m below the surface.

3.2. Shallow seismic velocity structure

Standard compressional (P) and shear (S) wave refraction methods were applied at the site to determine the seismic velocity structure. A linear array of 24 geophones spaced 1 m apart was arranged perpendicular to the test track. Hammer blows were then recorded at intervals off each end of the array. The resulting distance vs. travel time curves were analyzed using the intercept time method to determine the seismic velocity as a function of depth. For the P waves, vertical sledgehammer blows on a metal plate at the ground surface were used as the source, and Mark Products Model L15-B vertical-component geophones with resonant frequencies of 4.5 Hz were used to record the resulting ground motion. For the S waves, a 0.2×0.2 m wooden plank was aligned perpendicular to the array and clamped to the ground by the front wheels of a pickup truck (Fig. 7). Horizontal sledgehammer blows on each end of the plank, which excited SH (shear horizontal) waves of opposite polarity, were then recorded at each source location using horizontal-component geophones.

One difficulty encountered was caused by the

Table 1. Borehole soil log.*

Layer	Depth to bottom of layer (m)	(ft)	Thickness of layer (m)	(ft)	Soil type
1	3.4	11	3.4	11	Medium sand
2	4.9	16	1.5	5	Fine gravel
3	5.8	19	0.9	3	Medium sand
4	7.6	25	1.8	6	Medium sand and water
5	7.9	26	0.3	1	Clayish fine sand
6	23.2	76	15.2	50	Medium sand and water
7	23.5	77	0.3	1	Blue clay
8	23.8	78	0.3	1	Medium and sand water
9	24.4	80	0.6	2	Blue clay
10	24.7	81	0.3	1	Brown clay
11	27.4	89	2.7	9	Medium sand and water
12	29.3	96	1.8	6	Clean sand and water
13	30.5	100	1.2	4	Medium sand and water with clay trace in water

*From Hal Carlson, Jim's Well Drilling, Grayling, Michigan.

presence of the frost layer. For recordings made close to the hammer source, the first arrival was a wave traveling directly through the frost layer, at a speed of about 590 m s^{-1}. Fortunately, this arrival was highly attenuated and died out within a few meters. We were able to pick the travel times of the later-arriving refracted waves after this first arrival and use them in the analysis. The P-wave velocity of the thin snow layer was measured at about 100 m s^{-1} by a short line of geophones placed above and below the snow cover and spaced 0.25 m apart. The measured first arrival travel times for the P- and S-wave refraction experiments along with least-squares line fits are shown in Figures 8 and 9.

Analysis of the travel times indicates a surface layer 4.8 m thick with a P-wave velocity of 290 m s^{-1}, underlain by a layer with a velocity of 1660 m s^{-1} that is identified as the water table. The shear wave data reveal a surface layer with a velocity of 150 m s^{-1}, 12 to 15 m thick, sloping downward at an angle of about 9 degrees to the north, above a layer

Table 2. Physical properties of borehole soil samples.

Sample no.	Depth (m)	(ft)	Description	Density (kg m^3)	Moisture content (%)	Percentage of soil type: Gravel fine	Sand coarse	Sand medium	Sand fine	Clay
1	1.5	5	Sand	1.38	3.7	7.6	1.8	34.5	63.5	0.3
2	3.0	10	Sand	1.45	3.4	4.6	2.0	33.0	63.9	1.0
3	4.0	13	Sand and gravel	1.56	2.8	18.2	10.2	35.7	35.6	1.1
4	6.1	20	Sand (below water table)	1.45	3.4	0.4	0.3	12.9	86.7	0.4
5	13.7	45	Sand	1.45	19.2	0.0	0.2	10.0	88.1	1.7
6	22.9	75	Blue clay	—	23.2	0.0	0.1	7.1	53.4	39.4
7	24.4	80	Brown clay	—	6.8	0.0	0.1	4.4	35.5	60.0
8	30.5	100	Sand with clay	1.73	19.4	0.0	0.0	15.0	75.7	9.4

The percentage of gravel, sand, and clay in each sample was determined from the grain size measurements. According to the unified soil classification scheme, soils with grains smaller than 9.5 mm but larger than 2 mm are classified as fine gravel. Sand has grain sizes less than 2 mm and greater than 0.076 mm and is further divided into coarse, medium, and fine at the 0.59 mm and 0.25 mm sizes. Grains less than 0.076 mm can be either silt or clay, but are assumed here to be clay based on field observations of the samples.

Figure 7. Generating shear waves for the site characterization measurements. The cable leading from the sledgehammer allows the impact time to be recorded.

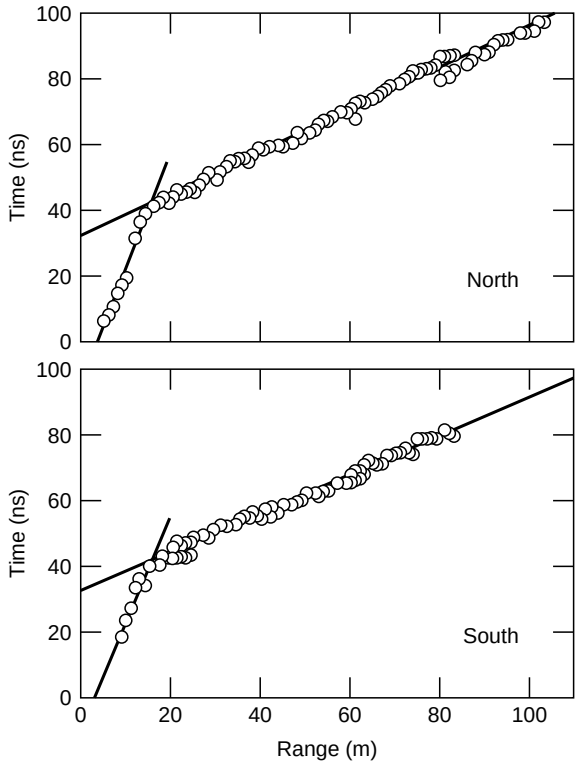

Figure 8. Compressional (P) wave refraction travel time vs. distance. The straight lines are least-squares fits to the travel time data. Shown are arrival times for waves from hammer sources located north and south of the linear array of geophones.

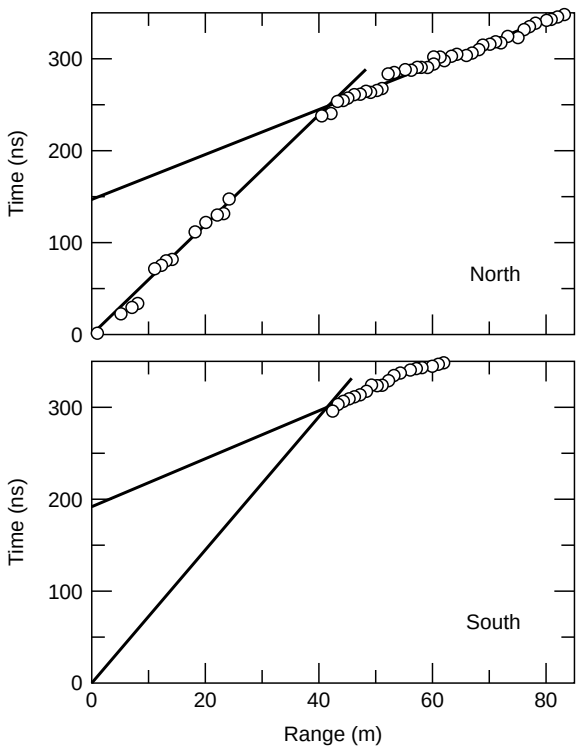

Figure 9. Shear (S) wave refraction travel time vs. distance. The straight lines are least-squares fits to the travel time data. Shown are arrival times for waves from hammer sources located north and south of the linear array of geophones.

Table 3. Analysis of seismic refraction travel time.

Layer	Apparent velocity ($m\ s^{-1}$) South	Apparent velocity ($m\ s^{-1}$) North	Intercept time (ms) South	Intercept time (ms) North	Velocity ($m\ s^{-1}$)	Depth (m) South	Depth (m) North	Dip angle (degrees)
				Compressional (P) waves				
1	276	301	0.0	0.0	288	4.78	4.80	
2	1584	1749	32.6	32.8	1662			–0.5
				Shear (S) waves				
1	167	137	0.0	0.0	152	12.2	15.7	
2	417	386	148.3	191.2	401			

with a speed of 400 m s^{-1}. Details of the intercept time analysis are given in Table 3. The seismic water table depth is about 1 m less than the well log depth, while the shear wave velocity change does not correspond to any obvious drill log layer. The vertical compressional and shear wave velocities of the shallow soil were also measured by clamping a three-component geophone at various depths in a cased, 30-m-deep borehole and recording the travel times of P and S waves from surface hits 3 m away from the top of the hole to the downhole geophone. The seismograms from the two downhole horizontal components of unknown orientation were rotated to the radial and transverse orientations before the first arrivals were picked. Figures 10 through 12 show the resulting travel time curves for the P and S waves, with least-squares line fits used to determine the velocities. These experiments indicate compressional wave velocities of 390 m s^{-1} at the surface, with a 1370-m s^{-1} layer below, starting at a depth of around 3 m. The measured shear wave velocity was 180 m s^{-1} at the surface and 340 to 380 m s^{-1} at a depth of 12 to 16 m. These results agree with the

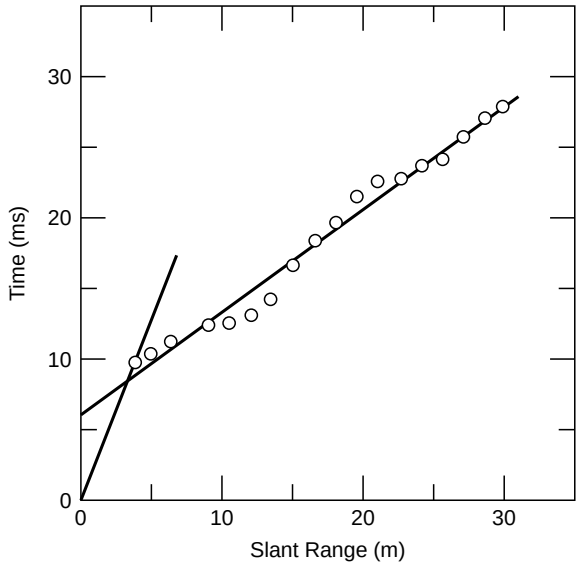

Figure 10. Compressional (P) wave downhole travel time vs. distance. Straight-line ray paths were assumed to calculate the slant distance from the measured sensor depth and horizontal source offset. These lines yielded values of 390 m s^{-1} down to 3 m, underlain by a velocity of 1370 m s^{-1}.

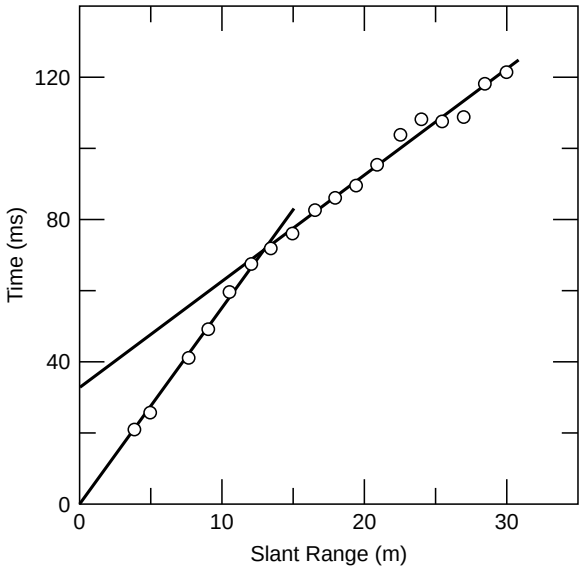

Figure 11. Transverse shear (S) wave downhole travel time analysis. The least-squares lines give 180 m s^{-1} down to 12 m and 340 m s^{-1} below that depth.

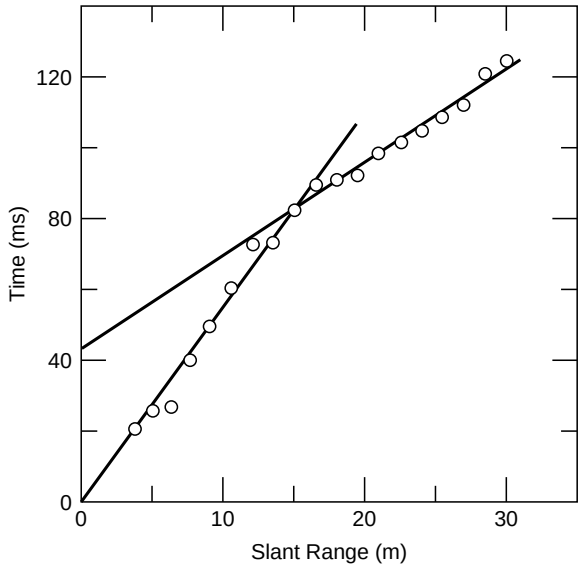

Figure 12. Radial shear (S) wave downhole travel time analysis. A velocity of 180 m s^{-1} down to 16 m, with 380 m s^{-1} below that, is indicated by the least-squares line fit.

refraction results discussed above. The average velocities over the upper 30 m were 1090 m s^{-1} for the P waves and 250 m s^{-1} for the two S waves.

3.3. Environmental characterization

A number of meteorological parameters were recorded continuously at the site of the seismic and acoustic experiments. A Campbell Scientific Inc. (CSI) Model 21X Micrologger was used to collect the data (Fig. 13), which were recorded on a cassette magnetic tape and written on a paper tape. CSI Model 107 thermistors recorded the temperatures in the ground, in the snow, and at heights of 0.01, 0.1, 0.3, 1, and 1.4 m above the snow. These readings have an accuracy of ±0.2°C. A CSI Model 207 sensor provided the temperature and relative humidity at a height of 2 m. The wind speed and direction at a height of 3 m was recorded by Met One Model 014A and 024A sensors with an accuracy of ±2% and ±5%, and a YSI Model 2014 barometer provided the barometric pressure to within 1 mb. Readings from the 12 sensors were taken every minute, and the average and standard

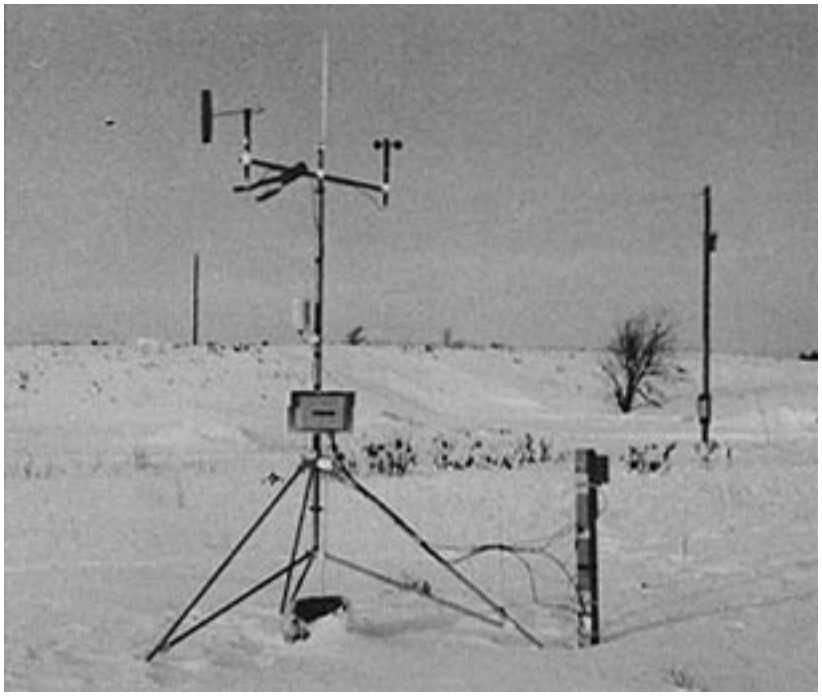

Figure 13. The instrumentation used to record meteorological parameters. The Campbell micrologger is housed in the box at the center of the tripod. At the top are the wind speed and direction sensors. The radiation shield contains a thermistor and the relative humidity sensor. Additional thermistors and a barometer are mounted on the wooden post. A lead–acid battery below the tripod provided the power.

Table 4. Meteorological data.

		Temperatures (°C)								Pressure	RH	WS	WD
Date	Time	Gnd	Snow	0.01 m	0.1 m	0.3 m	1 m	1.4 m	2 m	(mb)	(%)	(m s^{-1})	(deg)
16 Feb	1630	–3.4	–3.4	–3.9	–4.2	–4.4	–4.2	–3.5	–4.5	963.6	94	3.3	201
16 Feb	1700	–3.3	–3.4	–4.0	–4.2	–4.4	–4.2	–3.5	–4.4	963.8	93	4.0	209
16 Feb	1730	–3.3	–3.4	–5.2	–5.0	–5.2	–5.0	–3.7	–4.9	963.9	92	3.9	207
16 Feb	1800	–3.3	–3.4	–5.4	–5.1	–5.3	–5.2	–4.1	–5.1	963.9	92	3.0	203
16 Feb	1830	–3.3	–3.4	–5.5	–5.1	–5.4	–5.3	–4.4	–5.2	964.0	92	2.7	222
16 Feb	1900	–3.3	–3.4	–5.5	–5.2	–5.5	–5.4	–4.6	–5.3	964.0	93	3.0	195
17 Feb	1100	–2.7	–2.7	–1.8	–1.2	–1.3	–0.8	0.0	–1.5	971.1	80	3.1	267
17 Feb	1130	–2.7	–2.7	–1.9	–1.1	–1.1	–0.8	0.3	–1.4	971.5	80	3.5	311
17 Feb	1200	–2.7	–2.7	–2.2	–1.7	–1.8	–1.5	–0.2	–1.7	971.5	81	5.1	306
17 Feb	1230	–2.6	–2.6	–1.2	–0.7	–0.7	–0.2	0.1	–1.4	971.8	76	5.3	286
17 Feb	1300	–2.6	–2.5	–2.2	–1.5	–1.7	–1.2	0.4	–1.4	971.8	76	4.5	302
17 Feb	1330	–2.5	–2.5	–2.5	–1.6	–1.6	–1.2	0.7	–1.6	971.7	74	6.4	256
17 Feb	1400	–2.5	–2.4	–1.2	–0.3	–0.1	0.3	0.9	–1.2	971.8	74	4.7	272

deviation of the values were computed and recorded every 30 minutes. The meteorological data recorded on 16 and 17 February 1988 during the seismic and acoustic array experiments discussed in this report are tabulated in Table 4. Two frost tubes were installed at the site in January: one was located 5 m north of the met station in a topographic high, and the second was located 10 m south of the met station in a topographic low. The elevation difference between the two was 0.95 m. The snow depth at the first frost tube was 0.14 m, and frost depth exceeded the depth of the tube (0.775 m) for all of the February readings. On 16 February, the snow depth at the second tube was 0.18 m and the frost depth was 0.60 m. Snow depths at the site during these experiments ranged from 0.14 to 0.20 m in most locations. The snow had been on the ground for some period of time. A snow pit examined on 18 February revealed the presence of a thin wind crust at the top underlain by rounded snow crystals with a layer of depth hoar at the bottom (Table 5).

3.4. Array description and recording procedures

All the waveform data were digitally recorded by a Geosource DSS-10A system on 9-track magnetic tape at 1600 bpi in the SEG B format. The recording system has a dynamic range of 90 dB and a bandwidth from 3 to 500 Hz at a sampling rate of 2 kHz. Mark Products L-15B vertical- and horizontal-component geophones with a resonant frequency of 4.5 Hz and a sensitivity of 32 V m s^{-1} were used to detect the ground motion. Globe 100C low-frequency microphones with a sensitivity of 2 V Pa^{-1} were also used as sensors. The geophones and microphones were placed in an 18-

Table 5. Snow characterization, pit 2, at 1020 on 18 February 1988.

Layer	Depth (mm)	Density (kg m^{-3})	Temperature (°C)	Hardness index	Crystal size (mm)	Crystal type
1	0		–3.5			Wind crust (irregular, broken crystals), planar dendrites
	1	120	–3.5	60	0.5	Rounded, often branched
	35	150	–5.0	5	0.5	Rounded, often branched
	85	210	–6.5	10	0.5	Rounded, often elongated
2	115		–5.0	0	2.5	Depth, hoar, angular, stepped grains
	140	160	–4.5		2.5	Depth, hoar, angular, stepped grains
	165		–4.5		2.5	Depth hoar, angular, stepped grains

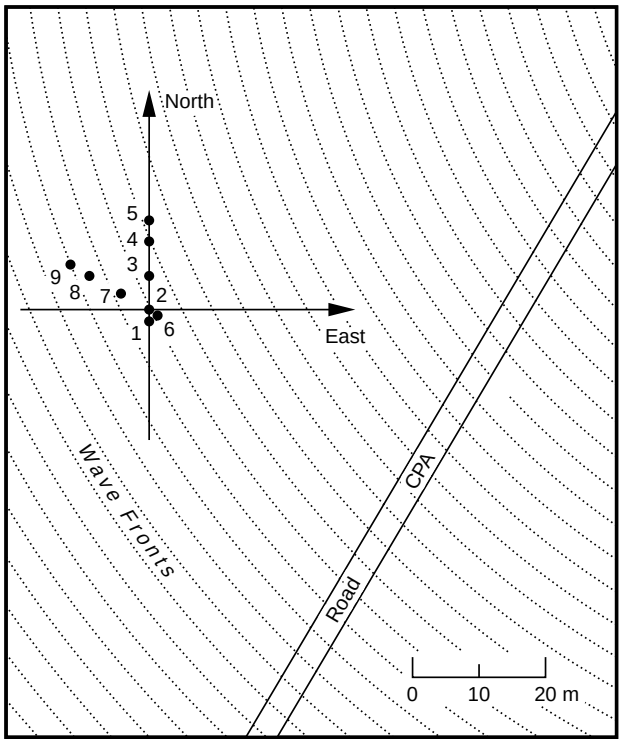

Figure 14. Grayling sensor positions and road, drawn to scale. Relative sensor coordinates and associated channel numbers are given in Table 6. North is referenced to the magnetic pole. Dots (•) are sensor locations.

element crossed array with one of the legs perpendicular to the test track. Figure 14 shows the sensor positions, and Table 6 gives the relative element positions. The array was calibrated by vertical hammer blows and blank pistol shots from five locations along the test track: at the closest point of approach of the vehicle (CPA), and at 50 and 100 m on either side of the CPA. Shear waves from the CPA were also recorded, as were pistol shots 50 m from the array center at the remaining compass points.

Table 6. Seismic array element position.

Element	*E to W (m)*	*N to S (m)*
1	0.0	–2.0
2	0.0	0.0
3	30.0	6.0
4	0.0	12.0
5	0.0	16.0
6	1.73	–1.0
7	–5.0	3.0
8	–10.4	6.0
9	–13.8	8.0

3.5. Characterization of the Grayling array

An important factor in qualitatively assessing the reliability of an estimated wavenumber spectrum based on the BT or ML methods is the presence of the array factor [$F(\vec{k})$] in the estimate. The array factor is the zero-phase impulse response for a given array geometry. The array impulse response provides important information on the direction-dependent resolution capability of the array as well as an estimate of the beam width for an ideal plane wave. It is a relatively simple matter to obtain such a response. The most straightforward method is given by

$$F(\vec{k}) = \frac{1}{M} \sum_{m=0}^{M-1} e^{-i\vec{k} \cdot \vec{R}_m}, \qquad (31)$$

which is simply a Fourier transform of the array element location vectors $\vec{R}_m$. The procedure used in this analysis is given by Kelley (1967) and differs from eq 13 only in that it allows for the analysis of a wideband array response based on a Gaussian distribution of zero-phase energy.

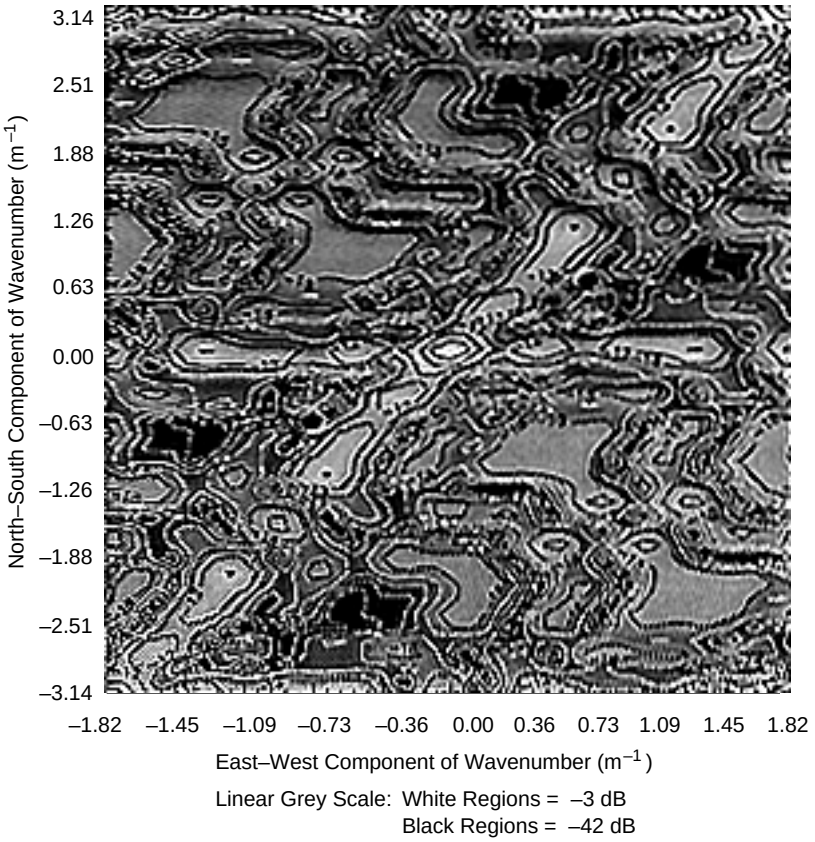

Figure 15. Grayling array impulse response. Plot ranges over k_x *and* k_y *Nyquist limits. Spectral resolution at –3 dB is 0.19 m^{-1}.*

The impulse response for the 1989 Grayling array is shown in Figure 15. The plot ranges to the Nyquist wavenumber limits along the x and y axes. The array factor is the x described by the –12-dB high-amplitude ridge lines radiating from the center of the plot. The inner contour at –3 dB defines the spectral resolution for this array, which is 0.19 m^{-1}. The high-amplitude lobes seen intruding from the periphery of the plot toward the center are grating lobes, which are a consequence of the periodic nature of the spectral estimation procedure.

The Grayling array geometry is not optimal with respect to multiple source resolution or providing equal resolution capabilities from all bearing directions. Signals arriving from directions in the vicinity of 0° or 180° and 55° or 235° will be poorly resolved. Maximum source resolution lies at directions perpendicular to these values. The element spacing of the Grayling array has been designed to allow coverage of a variety of possible wavelengths ranging from 4 to 30 m.

4. DISCUSSION OF SOURCE CHARACTERISTICS

To understand the direction estimates of moving seismic–acoustic sources it is instructive to first consider the spectral properties of simpler sources. We therefore begin by looking at impulsive acoustic and seismic wave fields generated by a .45 caliber (blank) pistol shot and a vertically delivered sledgehammer blow. The pistol shot was recorded around 1500 on 16 February, and the hammer blow around 1730 on the same day.

All estimates of the phase velocities discussed in this section are based on a time-domain moveout method. Each waveform in the time-domain signal vector is synchronized by specifying the source direction (θ) and phase velocity (V_o) of the waveforms. Since the spatial distribution of the array elements is known, we can calculate the relative differences in arrival times between all elements in the array. The time shift may be expressed as

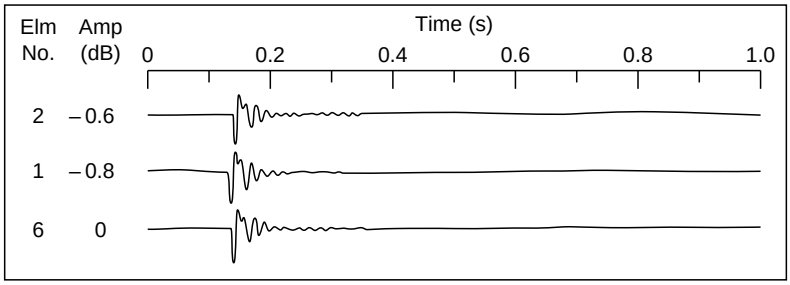

Figure 16. Microphone subarray response to a .45 caliber blank pistol shot.

$$\Delta t_m = \frac{\sqrt{x_m^2 + y_m^2}\cos\left(\alpha_m - \theta\right)}{V_o}, \qquad (32)$$

where α_m is the angular location of the mth sensor. Given a digital record of an ideal plane wave source, the accuracy of eq 32 will be limited by the time-domain sample interval.

4.1. Impulsive acoustic source

The first field example discussed is the .45 caliber pistol firing blanks toward the array from the closest point of approach (CPA). The time-domain microphone and geophone response to a single pistol shot are shown in Figures 16 and 17. The microphone waveforms have phase velocities of approximately 330 m s^{-1}. The seismic waveforms (Figure 17) have two distinct arrival phases. The first arrival is a roughly 75-Hz waveform that has a phase velocity of approximately 330 m s^{-1}. It has the distinct appearance of the acoustic impulse observed in the microphone waveforms. Later in the geophone time series, the waveforms shift to 25 Hz and have a phase velocity of approximately 220 m s^{-1}.

The frequency domain spectra for these signal vectors are given in Figures 18 and 19. Each spectrum is based on a 2000-point series sampled at 0.0005 s, segmented into 3 blocks of 1024 points, and overlapped by 53%. A Blackman window taper was applied to each block.

The primary features to note in the microphone

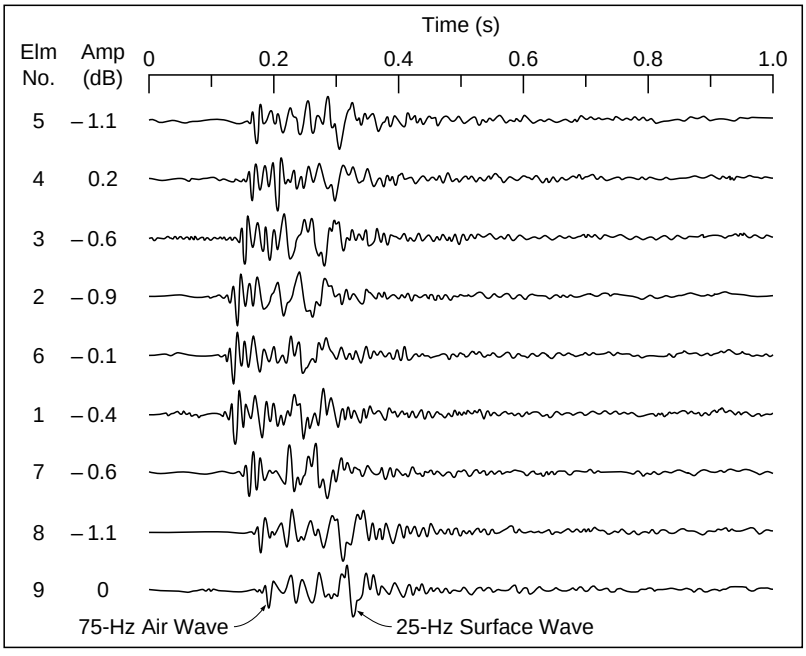

Figure 17. Time-domain vertical geophone subarray response to a .45 caliber blank pistol shot.

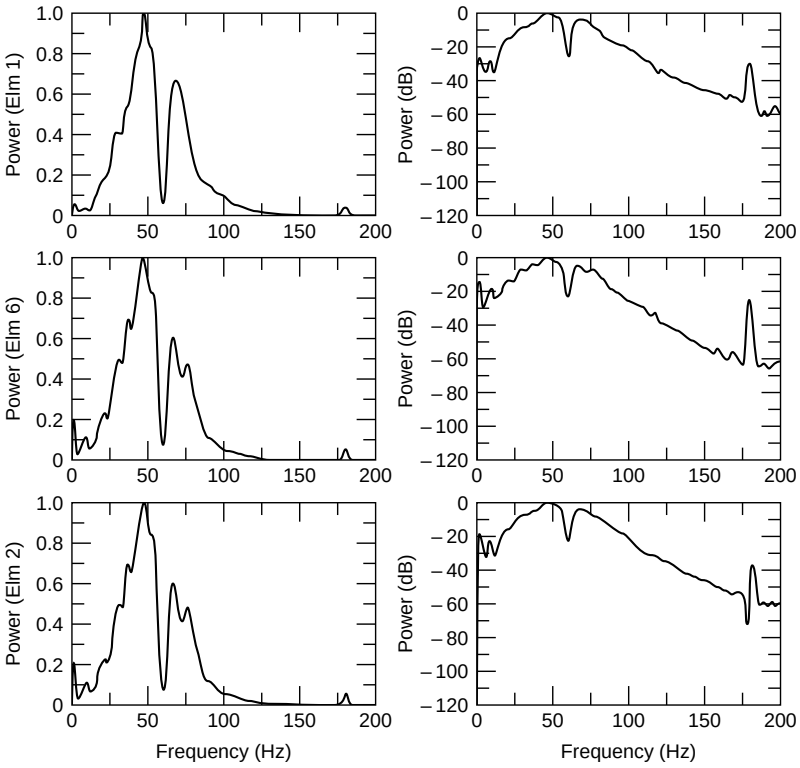

Figure 18. Microphone spectrum for .45 caliber pistol shot: (left) Linear scaling and (right) logarithmic scaling. The large spectral depression at 60 Hz is a result of notch filtering during the recording process. The 180-Hz peak is probably a harmonic.

spectra are the broadband nature of the signal and the presence of two high-amplitude bins at 45 and 70 Hz, separated by a deep spectral low around 60 Hz (produced from a notch filter). The appearance of the geophone response is considerably more complex and may be a result of several propagation factors such as modal effects associated with surface wave propagation and acoustic-to-seismic coupling. The majority of the energy in vertical-geophone spectra is contained in a band between

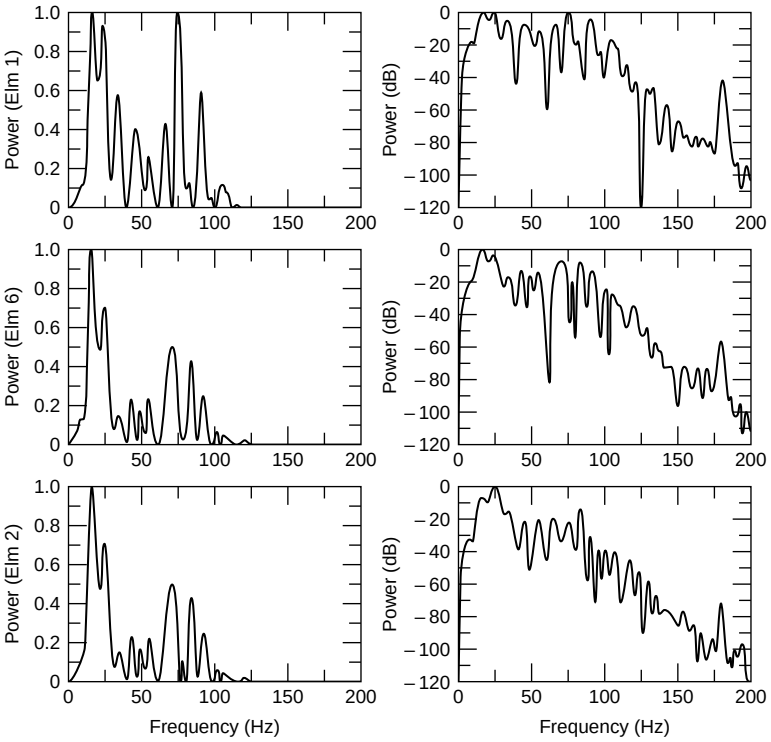

Figure 19. Spectra for three center elements of the geophone subarray for a .45 caliber pistol shot.

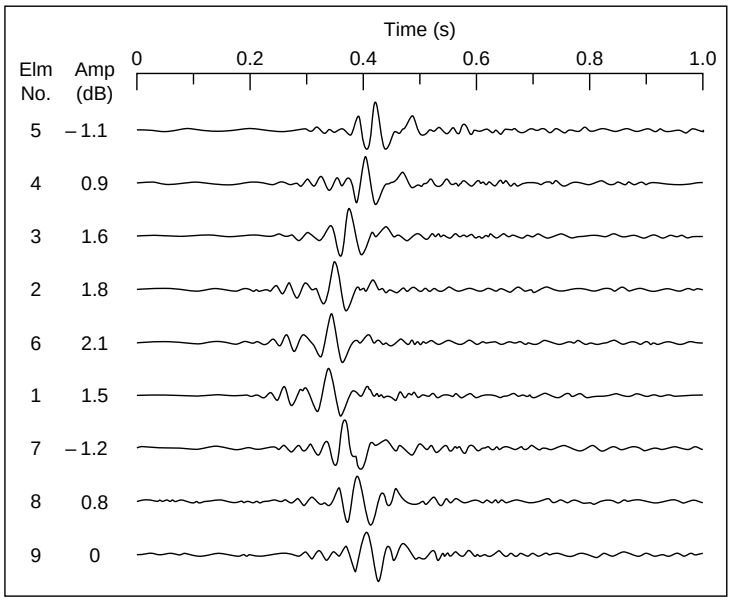

Figure 20. Vertical geophone subarray response to a stack of eight hammer blows. The element number and peak-to-peak amplitude are listed to the left of each trace. The amplitudes are arbitrarily normalized to the trace from element 9.

10 and 30 Hz, with an additional spectral peak near 70 Hz.

4.2. Impulsive seismic source

Figure 20 shows a series of vertical-component geophone waveforms obtained by digitally stacking eight vertically delivered sledgehammer blows. The source position is located on the road at a point 50 m to the southwest of the CPA at a direction of –78°. Using eq 32 it is found that the phase velocity is approximately 220 m s^{-1}. The power spectra for the three center elements from this array (Fig. 21) indicate that the signal is broadband with peaks at 20 and 40 Hz.

The pistol and sledgehammer sources indicate that the dominant seismic energy carrier is a surface wave propagating with a phase velocity of approximately 220 m s^{-1} and having a mode frequency of between 20 and 30 Hz. Analysis of the pistol shot records clearly shows that high-energy acoustic sources couple strongly with the ground to produce surface waves. This is consistent with the previous findings of Albert (1989). In addition to the acoustically induced seismic surface wave, the geophone is also excited by the airborne pressure pulse. These propagation modes can interfere and may be a source of difficulty for beamforming processors.

4.3. Moving seismic–acoustic sources

Recordings of a tank were also made as a U.S. Army M60 tank was driven up and down the test track at various speeds. A malfunction with the recording equipment prevented continuous signatures from being obtained, so a series of 1-s-long signature snapshots was recorded. The 10 tank signatures examined here were recorded between 1256 and 1259 on 17 February.

We now discuss the spectral properties of an M60 tank moving at approximately 4.5 m s^{-1} (10 mph). The vehicle's direction (θ) during this record interval was approximately 260°. Figures 22 and 23 present the time-domain waveforms observed by the vertical-geophone and microphone subarrays, respectively. In the vertical-geophone waveforms there is a high degree of both temporal and spatial variation in the signals. The peak-to-peak amplitude variation across the array ranges up to 6.6 dB. Since the spatial variations between array elements were not consistent from record to record, it is unlikely that the variations are due to geophone coupling to the ground or to variation in the snow cover.

Spectra were estimated using a total signal length of 2000 points segmented into three blocks of 1024 points. Each block is overlapped by 53% and tapered using a Blackman window. Figure 24

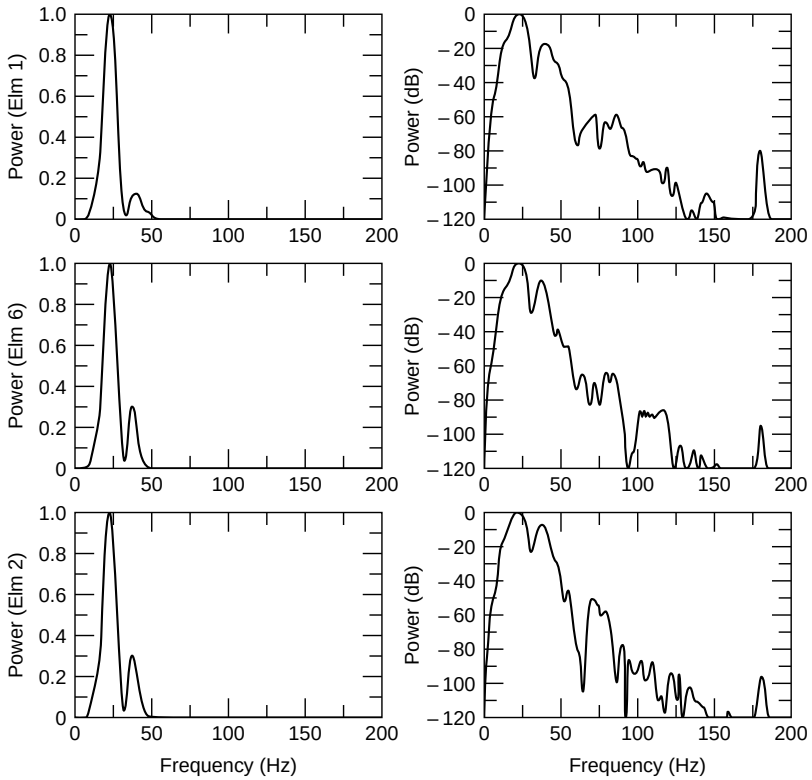

Figure 21. Hammer blow spectra from center array elements for vertical geophone subarray.

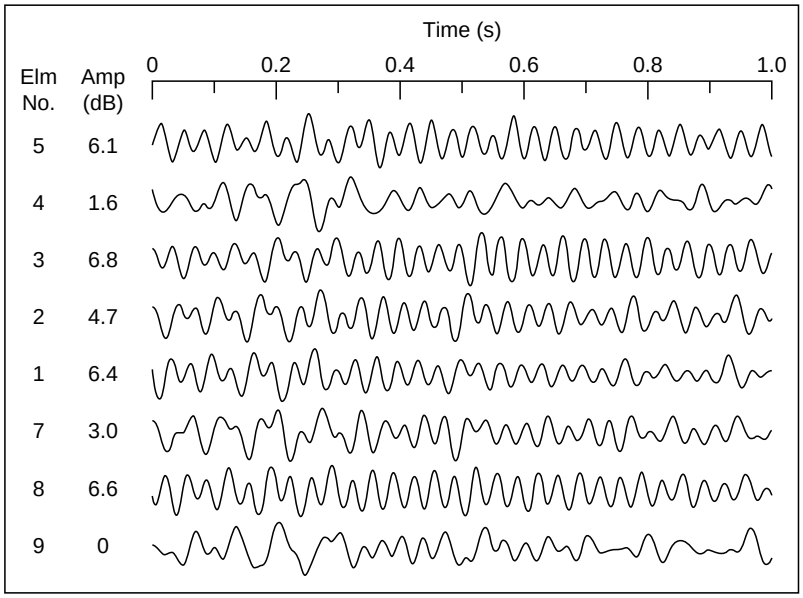

Figure 22. Time-domain vertical geophone subarray response to M60 tank moving at 4.5 m s^{-1}.

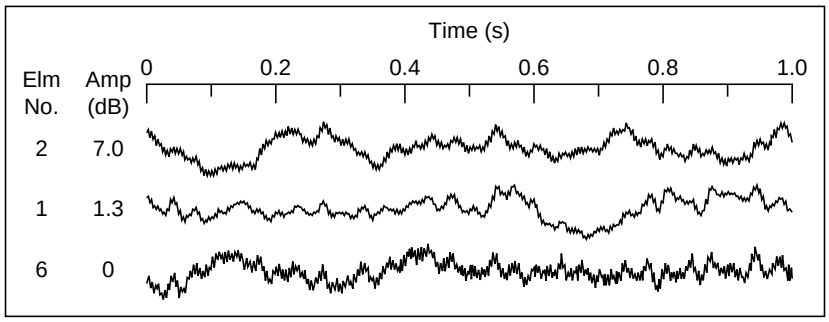

Figure 23. Time-domain microphone subarray response to M60 tank moving at 4.5 m s^{-1}.

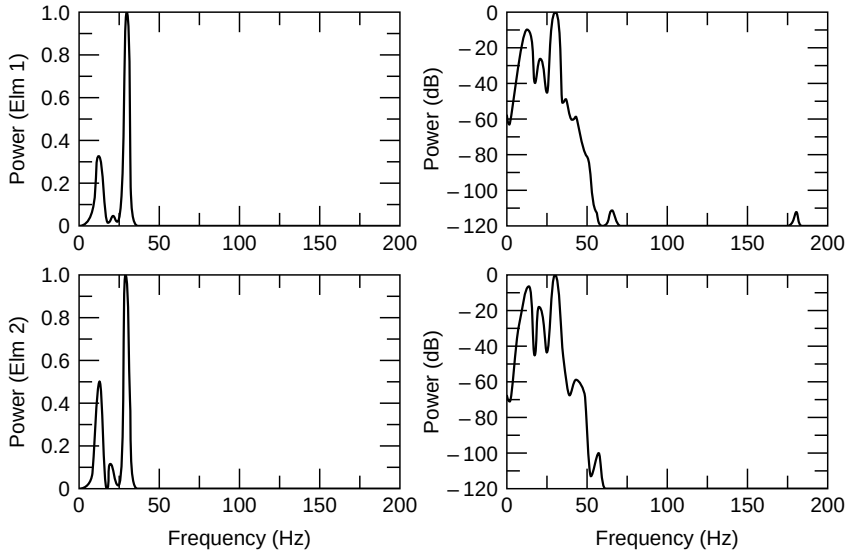

Figure 24. Spectra of two center elements of vertical geophone subarray for an M60 tank moving at 4.5 m s^{-1}. Spectra are strongly peaked at 11 and 29 Hz.

shows the vertical-geophone power spectra of elements 1 and 2 from Figure 22. The spectra are strongly peaked at 11 and 29 Hz. Plane-wave modeling at these two frequencies with a phase velocity of 220 m s^{-1} and the Grayling array geometry indicates that signal interference may be the cause of the amplitude variation across the array. Interference effects may also be present between acoustic energy coupled near to the geophone and surface waves excited near the source. This hypothesis is partially supported by the presence of a strong spectral peak at 29 Hz in both the microphone and vertical-geophone spectra (Figures 24 and 25).

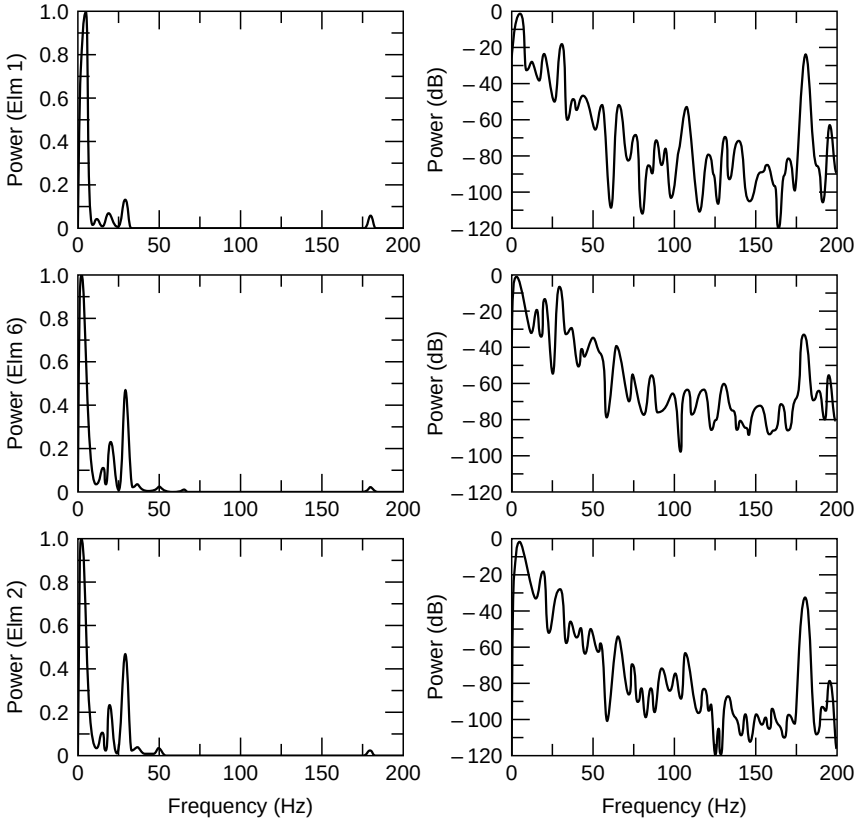

Figure 25. Spectra of microphone subarray response to an M60 tank moving at 4.5 m s^{-1}. Spectra are strongly peaked around 3 Hz and 29 Hz.

5. PROCESSING RESULTS FOR FIELD RECORDS

This section presents ML wavenumber estimates of Grayling field data for the .45 caliber blank pistol, the sledgehammer, and the M60 tank moving at 4.5 m s^{-1}. All wavenumber estimates were formed over a regular grid space containing 2601 points. All spectral estimates contain various degrees of bias and variance. To demonstrate the degree to which frequency domain bias and variance can affect wavenumber estimates, we show several results that use different OBAFFT parameters on the same M60 signal vector.

5.1. Criteria used to select processed frequencies

Several criteria were used to select the frequency bin at which a wavenumber estimate is formed. The most important of these processing criteria was the average array coherence spectra, which is formed by calculating and summing the magnitude-squared coherence spectra (Γ_{ave}) between all possible channel combinations and then normalizing by the number of combinations. This operation is given as

$$\sum_{j=i+1}^{M} \frac{\left|\hat{X}_i^{\ell}(f) \bullet \hat{X}_j^{*\ell}(f)\right|}{\left|\hat{X}_i^{\ell}(f)\right|\left|\hat{X}_j^{\ell}(f)\right|}$$

$$\hat{\Gamma}_{ave} = \frac{2}{(nblks)\left(M^2 - M\right)} \sum_{\ell-1}^{nblks} \sum_{i-1}^{M-1} \tag{33}$$

In general, wavenumber spectra which were processed at frequency bins with coherences greater than 0.65 and a coherence variance across immediately adjacent bins of less than 0.025, produced reasonable wavenumber estimates. However, it was found that wavenumber estimates could still vary by a considerable degree even with average coherences of 0.9 (usually this was accompanied by high coherence variance across adjacent bins). Such variation can be explained by recognizing that the coherence spectrum is also susceptible to bias and variance errors.

The average array coherence spectrum is strongly affected by the OBAFFT parameters. The Blackman taper normally produced a smoothly varying coherence spectrum with peaks ranging over several frequency bins. In contrast, a boxcar taper often produced an erratic coherence spectrum. In general, peaks in the coherence spectra greater than 0.7, which varied smoothly through several bins, produced acceptable wavenumber estimates. Wavenumber estimates based on seismic signals from the moving tracked vehicles tended to be reliable at frequencies between 9 and 15 Hz despite the occurrence of peak spectral energies in the vicinity of 30 Hz. The 30-Hz bins rarely produced satisfactory wavenumber estimates.

Several factors were useful in qualitatively determining the accuracy of wavenumber spectra. The most important was the presence of a strong array factor. This was particularly relevant when assessing the quality of wavenumber estimates based on small numbers of OBAFFT blocks. Another key indicator proved to be the estimate of the phase velocity. An estimated phase velocity consistent with the surface wave velocity found by the time-domain move-out analysis was usually a good indicator of an accurate wavenumber estimate. In addition, if the spatial correlation is normalized according to eq 25 then, when using the Bartlett method, a peak power value of 0.6 or greater often accompanied an accurate estimate.

5.2. Impulsive sources

The first series of wavenumber estimates is based on the vertical-geophone subarray response to the .45 caliber blank fired from the CPA at θ = –40°. The waveforms of this signal vector are shown in Figure 17. Figure 26 shows the average array amplitude and coherence spectra, based on a 2000-point series with three blocks. Each block contains 1024 points, is overlapped by 53%, and is tapered using a Blackman window

Recall from section 4 that there are two distinct arrivals in this record. The wavenumber estimate shown in Figure 27 is the Capon maximum-likelihood estimate processed at 78 Hz. This frequency was chosen since it produces a wavelength comparable to the spacing of the center elements of the geophone array with an acoustic propagation velocity. The time-domain interval considered was between 0.1 and 0.25 s. This corresponds to a time window that brackets the initial impulsive arrival seen in Figure 17. There were 230 sample points in this interval. The estimate was formed using a block length of 128 points with each block overlapped 60%, giving a total of three blocks. Boxcar windowing was applied. The coherence at 78 Hz was 0.7. The wavenumber spectrum (Fig. 27) produces an estimated source direction of –40° and a phase velocity of 338 m s^{-1}. This is consistent with the direction of the pistol shot and the acoustic propagation velocity. Note that the convention followed plots the true vector orientation of the

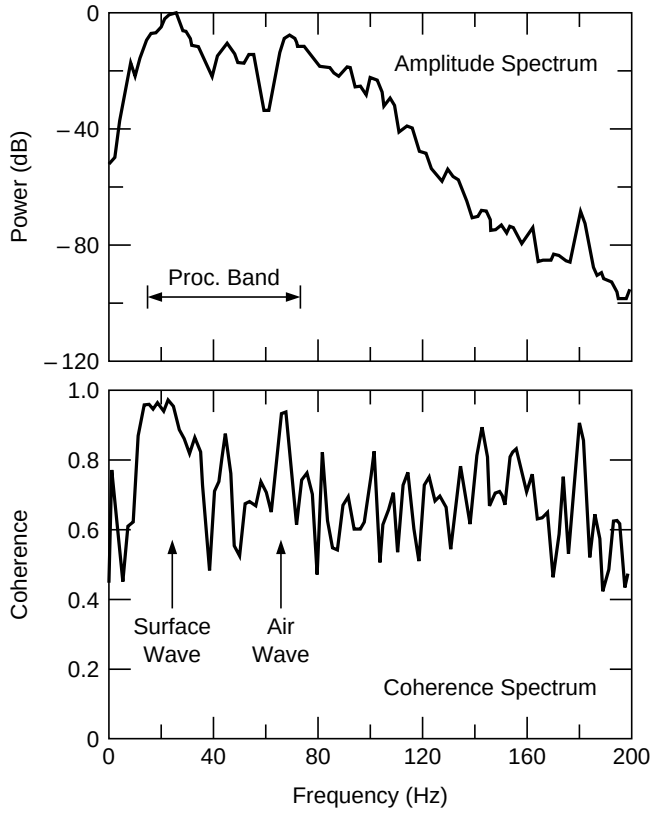

Figure 26. Average array spectra for vertical geophone subarray to .45 caliber pistol shot.

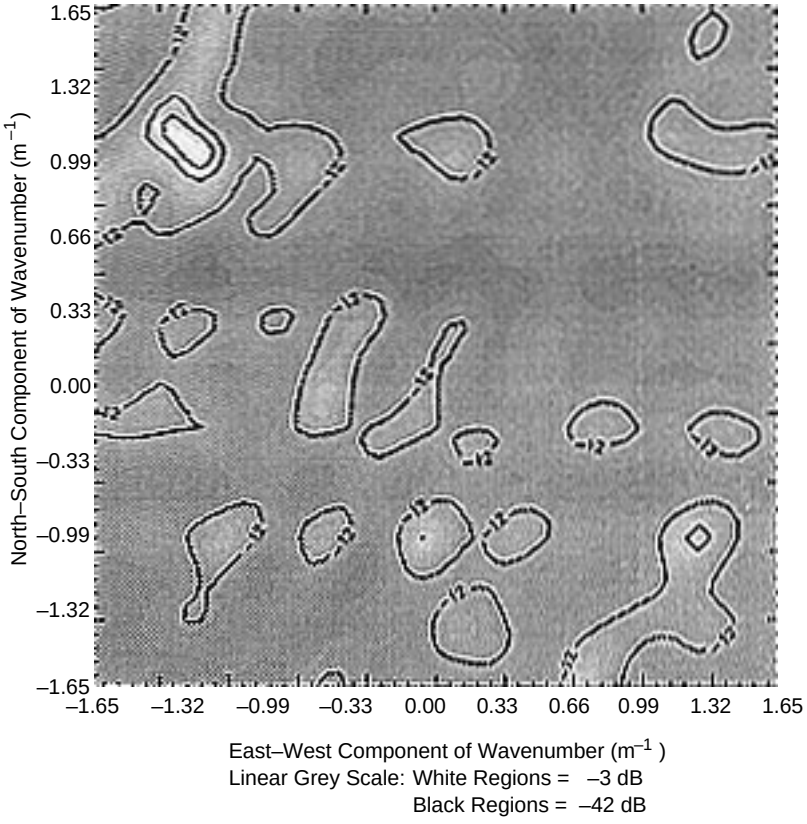

Figure 27. ML wavenumber spectrum at 78 Hz for vertical geophone subarray. The location of the spectral maxima indicates a source direction of $\theta = -40°$ and a phase velocity of 338 m s^{-1}.

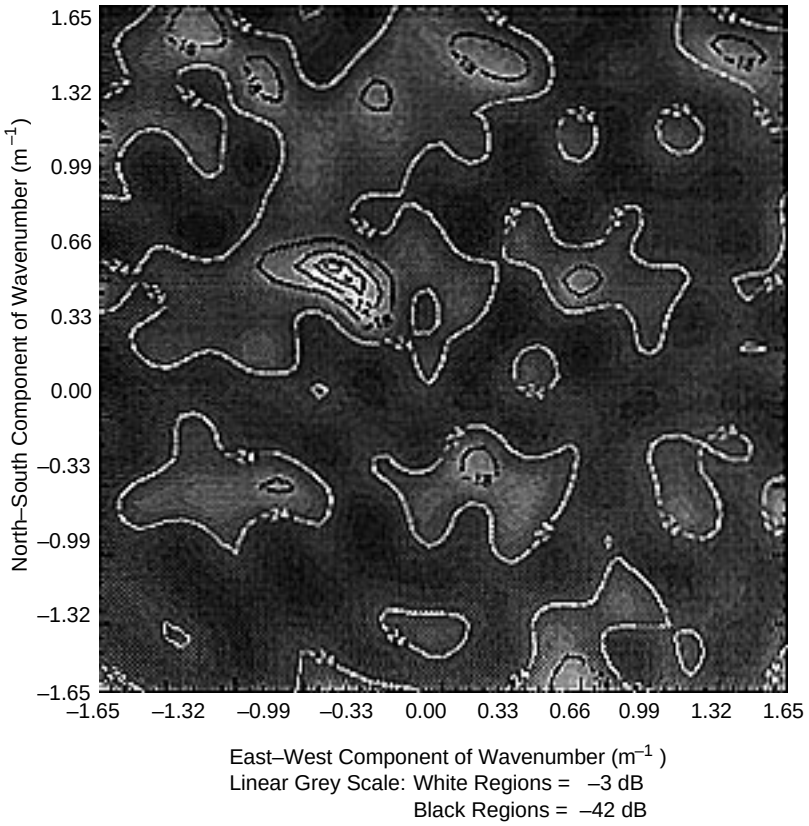

Figure 28. Estimated ML wavenumber spectrum at 23 Hz for vertical geophone subarray. Location of spectral peak gives a source direction of $\theta = -37°$ and a phase velocity of 223 m s^{-1}.

wavenumber. Thus, all incoming source wavenumbers are oriented 180° away from the source direction.

Figure 28 is a 23-Hz ML wavenumber estimate of the same pistol shot record. The time interval considered encompasses the later portion of the wave train between 0.2 and 0.5 s. There were 500 points in this interval. The time-domain move-out analysis indicated a phase velocity of roughly 220 m s^{-1} in this interval. A block length of 256 points overlapped by 60% was used, giving four blocks in the estimated spatial correlation matrix. A boxcar window taper was applied. The average array coherence in the 23-Hz bin was 0.8. The wavenumber spectra in Figure 28 give a source direction of $\theta = -37°$ and a phase velocity of 223 m s^{-1}. These values agree with the known source direction and the time-domain estimates of the propagation velocity.

The last beamformer response for the pistol shot is shown in Figure 29. This is a broadband ML estimate processed on an 800-point time interval between 0.1 and 0.5 s. A block length of 128 points was chosen with no block tapering. The block overlap was 40%, giving nine blocks. The frequency band evaluated was from 15 to 78 Hz. Selection of these parameters allowed the spectral estimate of each block to retain a high degree of independence with emphasis on the resolution of specific frequency bins. In Figure 29 there are three spectral maxima that have energy levels greater than –3 dB. All three trend along a high-amplitude "ridge," indicating a source direction of roughly –40°. The wavenumber peak with the smallest magnitude yields a phase velocity of 223 m s^{-1} if normalized by a frequency of 23 Hz. The wavenumber peak with the intermediate magnitude yields a phase velocity of 342 m s^{-1} when normalized by 78 Hz.

The above series of wavenumber spectra and the time-domain plots clearly show the existence of an acoustically induced seismic surface wave. In considering the ML wavenumber spectra it should be remembered that the wavefield was generated by a nearly ideal stationary point source. The OBAFFT parameters used in the ML wavenumber spectra were chosen through trial and error, and in many circumstances reasonable parameters did not yield intelligible beam responses. The above set of wavenumber estimates (Fig. 27 to 29) serve as a testament to the impact of the frequency domain estimation methodology on

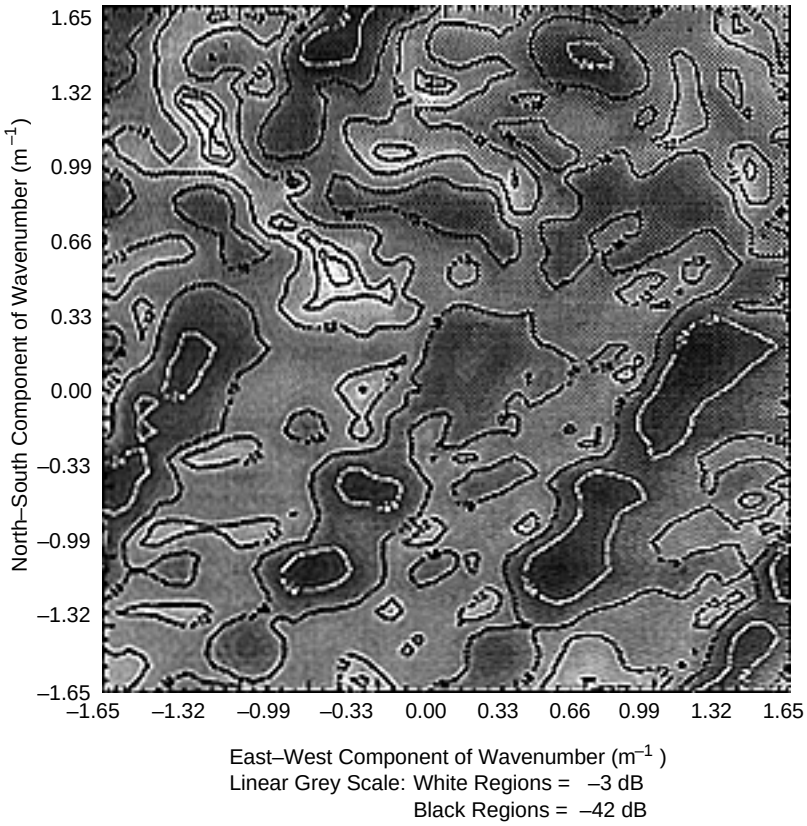

Figure 29. Broadband ML wavenumber spectrum for vertical geophone subarray. The processed frequency band is 15 to 78 Hz. High-amplitude linear ridge along a wavenumber space direction of 140° indicates a source position of –40°. The locations of spectral maxima indicate waves propagating at 223 and 342 m s^{-1}.

the resulting wavenumber spectra.

The next ML wavenumber spectra we consider are for the vertical-geophone signal vector produced by a vertically delivered sledgehammer blow (see Fig. 20). The source location was on the road 50 m south of the CPA at θ = –78°. Figure 30 displays the average array power and coherence spectra. The OBAFFT parameters used for the power, coherence, and wavenumber spectra were a signal length of 2000 points segmented into three blocks of 1024 points, each overlapped by 53% and tapered with a Blackman window. The 95% variance bounds were $\hat{\mathbf{R}} \bullet (0.46, 3.96)$ with 5.51 d.f. The 25-Hz ML wavenumber spectra based on this record are shown in Figure 32. The average array coherence at 25 Hz is 0.64. The location of the spectral maximum in the wavenumber estimate gives θ = –74° with a phase velocity of 232 m s^{-1}.

5.3. Moving sources

The first source we consider (Figure 22) is an M60 tank travelling along the road from southwest to northeast at 4.5 m s^{-1}. This was recorded when the vehicle was 300 m to the southwest of the CPA. The OBAFFT parameters used to produce the wavenumber, power, and coherence spectra

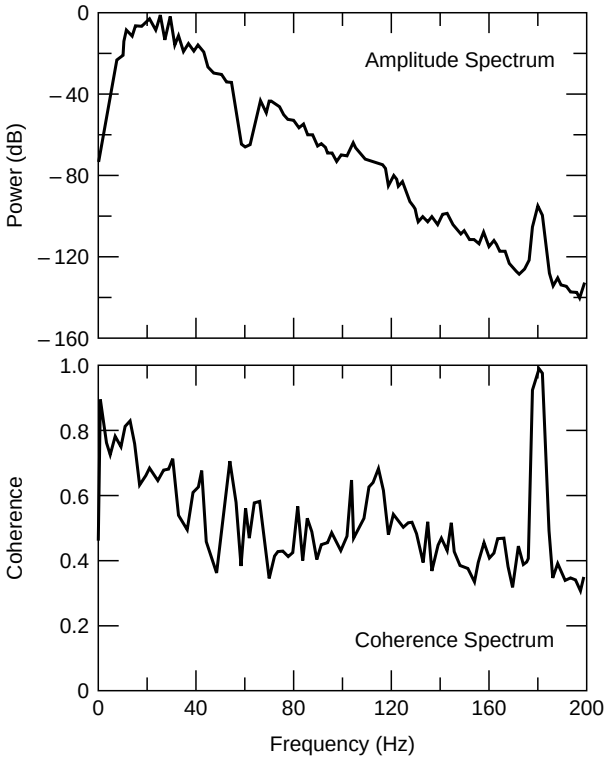

Figure 30. Average array spectra for vertical geophone subarray to stack of eight hammer blows.

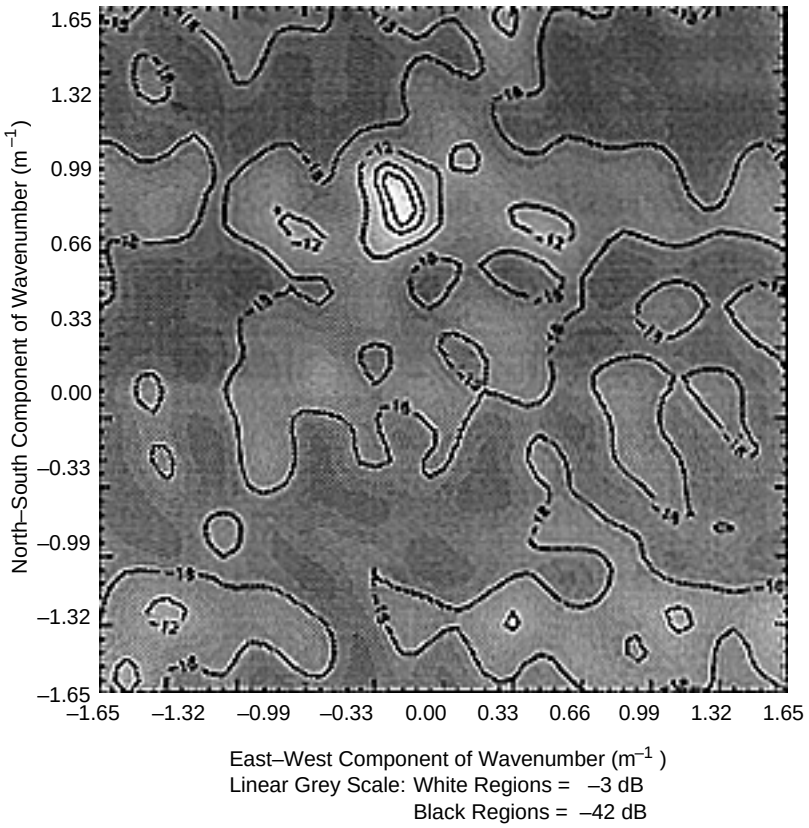

Figure 31. Estimated ML wavenumber spectrum at 25 Hz for vertical geophone subarray for hammer blows. Peak amplitude gives a source direction of $\theta = -74°$ and a phase velocity of 232 m s^{-1}.

are a series length of 2000 points segmented into three blocks of 1024 points, each overlapped by 53%, and tapered with a Blackman window function. The 95% confidence bounds are $\hat{\mathbf{R}} \bullet (0.46, 3.96)$ with 5.51 d.f. Figure 32 shows the average array power and coherence spectra. There is a peak in the power spectrum at 11 Hz that has a coherence of 0.94. The 11-Hz ML wavenumber spectrum (Fig. 33) estimates the source direction as $\theta = 258°$ with a phase velocity of 219 m s^{-1}.

The result shown in Figure 33 is typical of ML wavenumber estimates obtained from the M60 in the 9- to 15-Hz band using the vertical-geophone subarray. To demonstrate this, consider Figure 34, which is a composite of direction and velocity magnitudes estimated from ML wavenumber spectra for a consecutive series of M60 vehicle records. The location of each direction position is sequentially labeled 1 to 16. All records in this composite are from the same M60 drive-by series, with the tank moving from southwest to northeast along the road at a constant speed of 4.5 m s^{-1}. The most distant records in this series were at positions 1 and 16, which correspond to vehicle ranges of 500 and 300 m, respectively. At position 11 the tank is 50 m from the array's coordinate origin.

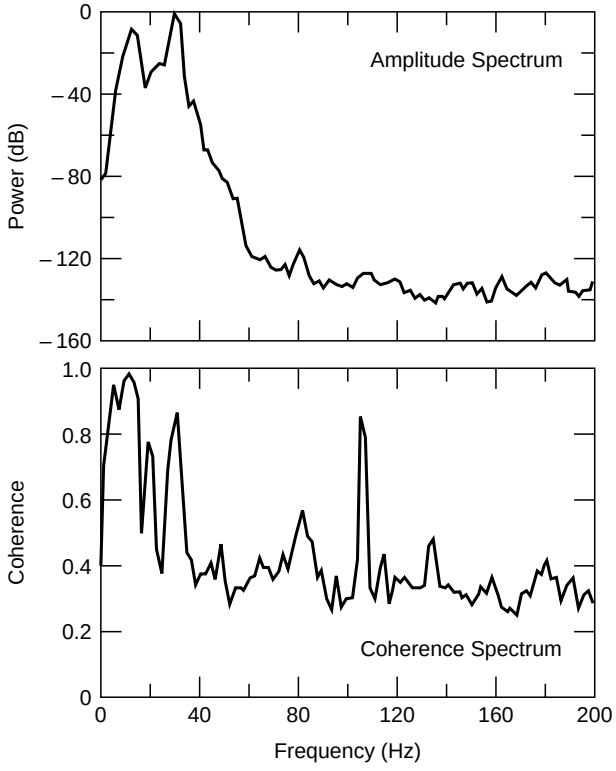

Figure 32. Average array spectra for vertical geophone subarray to M60 tank moving at 4.5 m s^{-1}.

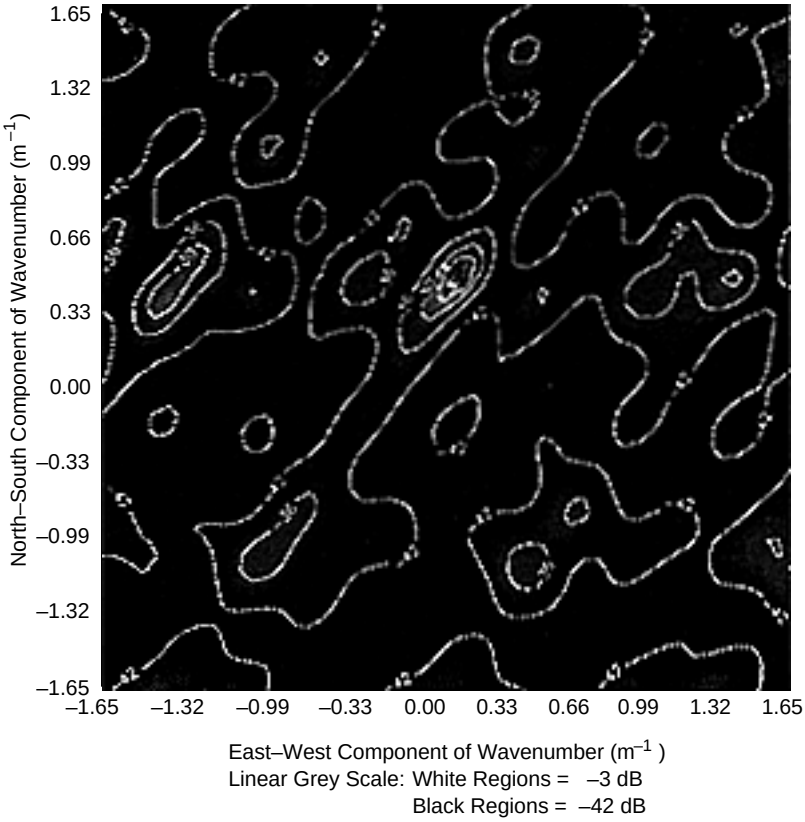

Figure 33. Example of an ML wavenumber estimate from a vertical geophone array at 11 Hz for an M60 tank moving at 4.5 m s^{-1}. Coherence was 0.94, the spectral maximum yields a velocity of 219 m s^{-1}, and the source direction = 258°.

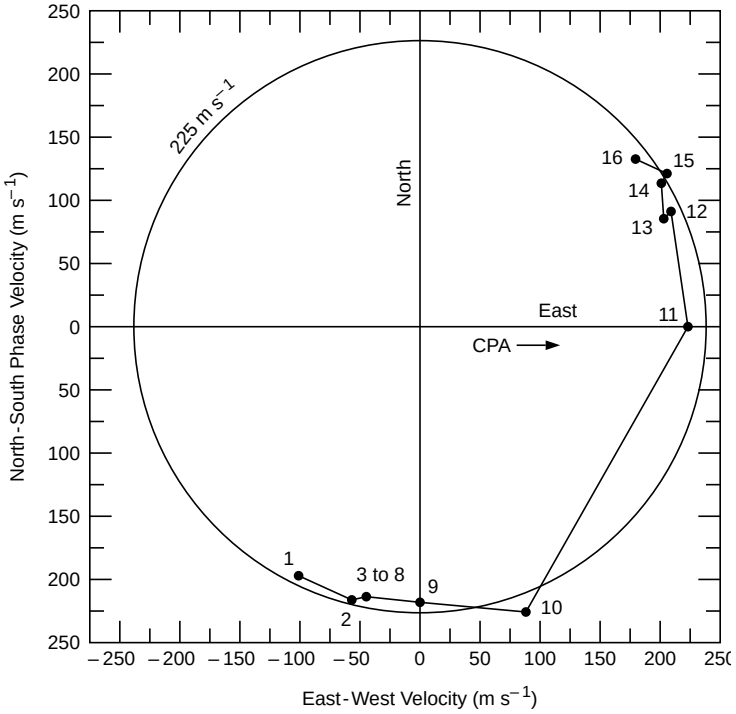

Figure 34. Composite plot of estimated source direction and velocity magnitudes for a series of M60 tank records observed by the vertical geophone subarray.

The composite uses a range of temporal frequencies from 9.77 to 29 Hz with the majority of the records using the 11-Hz bin. All the estimates used 2000-point signal lengths, segmented into three blocks of 1024 points, each overlapping the previous by 53%. A Blackman taper was used for 10 of the wavenumber estimates, with the remaining five estimates using a boxcar window taper. Using the boxcar window, the 95% confidence bounds on the crosspower matrix were $\hat{\mathbf{R}} \bullet (0.42, 5.85)$ with 3.9 d.f. The decision to use either a boxcar or Blackman taper was based on the coherence spectra and the consistency of the velocity estimates of the resulting wavenumber spectra.

5.4. Affect of spectral estimation parameters on beam response

In the preceding sections we demonstrated that ML wavenumber spectra from small seismic arrays can produce accurate direction estimates with careful choice of transformation parameters. Another result is that small differences in the frequency-domain processing parameters often have large effects on the wavenumber estimate. Such effects are termed a wavenumber bias. In this section several examples of the wavenumber bias phenomenon are demonstrated for the M60 tank.

When using reasonable OBAFFT parameters, the wavenumber bias effect was negligible for signal vectors observed from sledgehammer blows or blank pistol shots. Thus, the wavenumber bias problem is most likely associated with the characteristics of the M60. Given the difficulty in producing accurate wavenumber estimates from the vertical-geophone array in the 29-Hz peak power bin of the M60 source, and the coincident occurrence of large energy levels at 29 Hz in the microphone and geophone power spectra (Fig. 25 and 26), it is tentatively proposed that the bias effect may be aggravated by interference between surface waves and acoustic energy coupling near the geophone and source movement.

5.5. Spatial frequency bias from moving sources

To show how changes in processing parameters can affect wavenumber estimation for the moving M60, we consider a series of wavenumber estimates using the same data set but applying slightly different OBAFFT parameters. In each case it will be shown how the estimation parameters lead to biased wavenumber estimates or to a reduction in the SNR as measured by the background energy level of the wavenumber spectrum.

Consider the signal vector shown in Figure 35 for an M60 tank moving along the road at 4.5

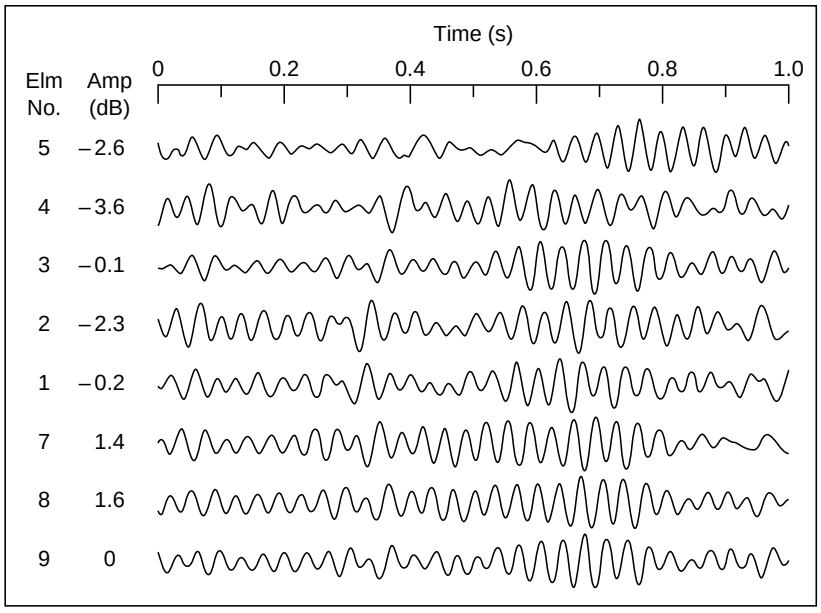

Figure 35. Time-domain response of vertical geophone subarray to M60 tank moving at 4.5 m s^{-1} along the road approximately 100 m southeast of the CPA. These waveforms correspond to position 8 in the composite plot shown in Figure 35.

m s^{-1} from southwest to northeast. An 11-Hz ML wavenumber spectrum is shown in Figure 36. It was formed using a series length of 2000 points segmented into 20 blocks; each block had 1024 points, was tapered by a Blackman window, and overlapped the preceding block by 95%. The 95% confidence bounds on the variance of the crosspower matrix was $\hat{\mathbf{R}} \bullet (0.38, 9.39)$ with 2.83 d.f. The average array coherence at 11 Hz was 0.92. The variance estimate leads one to expect that no significant improvement in the wavenumber spectra will result from such highly overlapped blocks. This is not the case, as will be shown later.

The wavenumber spectrum in Figure 36 is notable in several respects. It has an extremely sharp spectral maximum with background energy levels as low as –45 dB. The highest side lobe in wavenumber space is 30 dB below the maximum. The location of the spectral maximum gives a source direction of 258° and a propagation velocity of 219 m s^{-1}.

The ML wavenumber estimate shown in Figure 38 uses the same signal vector as that of Figure 36. In this spectrum the OBAFFT parameters are identical except the blocks are boxcar windowed. The variance estimate is $\hat{\mathbf{R}} \bullet (0.42, 5.83)$ with 3.89 d.f. at the 95% confidence level. In this extremely overlapped region the variance bounds are slightly better than those found for the Blackman window function used in the previous example. Figure 37 is a notable wavenumber estimate in that it has an exceptionally peaked spectral maximum, which indicates a source direction of 258° and a phase velocity of 219 m s^{-1}. There are several subtle differences between Figures 37 and 38. The first is the occurrence of a relatively pronounced spectral side lobe in Figure 37 that is 18 dB smaller than the spectral maximum. In addition, the background energy level in Figure 37 is approximately –33 dB while that of Figure 36 was approximately –45 dB.

The next two wavenumber estimates investigate the impact of reducing the number of blocks in the OBAFFT. In Figures 38 and 39 we process a signal length of 2000 points, blocked into segments of 1024 points, with each overlapped by 53%, giving a total of three blocks. In the case of Figure 38 we apply a Blackman window taper to each block, whereas the wave number estimate shown in Figure 39 used a boxcar window function.

In Figure 38 the spectral maximum is sharply peaked, indicating a source direction of 258° and a

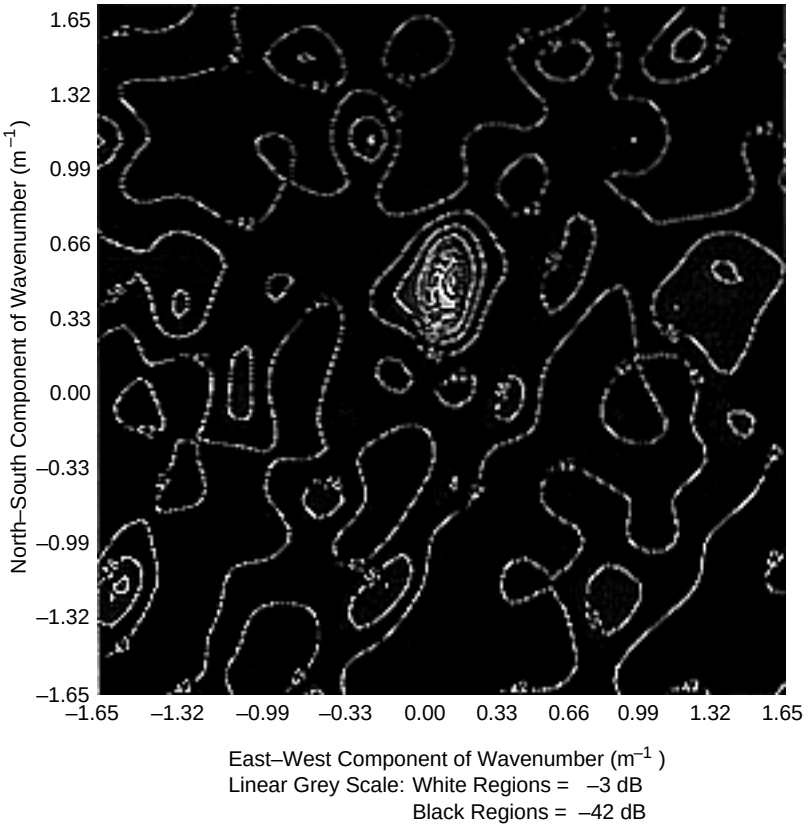

Figure 36. ML wavenumber estimate at 11 Hz for waveforms shown in Figure 35: Blackman taper, 20 blocks (at 95% overlap), segment length = 1024; produces a source direction of 258° with a velocity of 219 m s^{-1}.

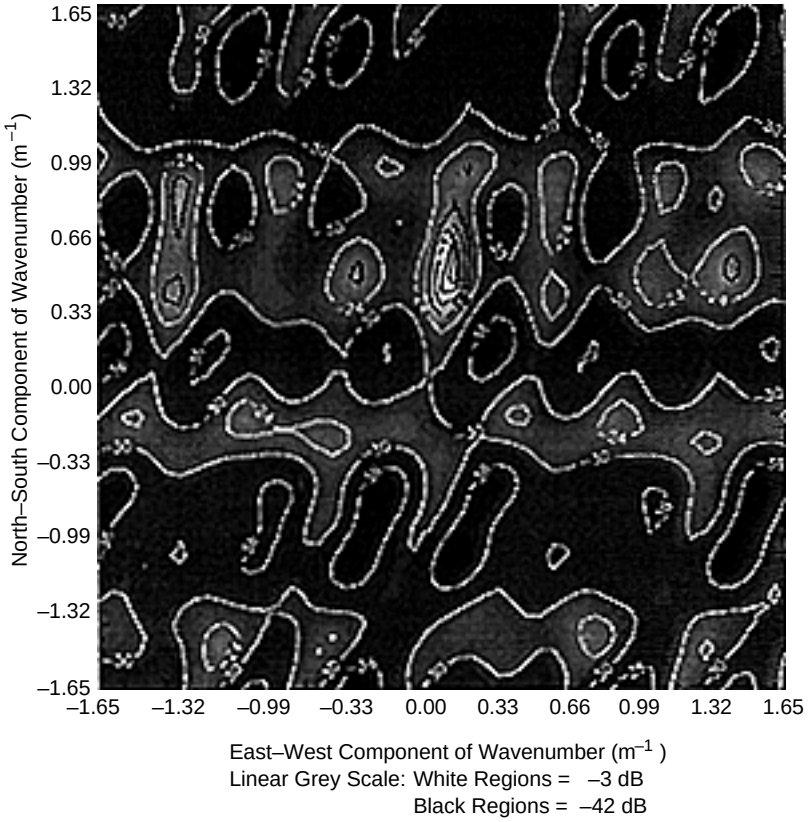

Figure 37. ML wavenumber estimate at 11 Hz for waveforms shown in Figure 35: boxcar taper, 20 blocks (at 95% overlap), segment length = 1024; produces a source direction of 258° with a velocity of 219 m s–1.

phase velocity of 219 m s^{-1}. The highest secondary side lobe is at –21 dB with an overall background energy level of –36 dB. In contrast, the wavenumber estimate shown in Figure 39 indicates a source direction of 255° and a phase velocity of 271 m s^{-1}. The 3° direction difference and 52 m s^{-1} velocity difference between Figures 38 and 39 is a mild example of the wavenumber bias effect. In addition, applying the boxcar window effectively reduces the SNR of the beamformer in the sense that the background energy level of Figure 38 increases by 6 dB in Figure 39.

Comparing Figures 36 and 37 with 38 and 39 we note that there seems to be significant benefit in using a larger number of highly overlapped blocks. Each estimate of the phase difference between two channels for a given block of data is calculated from a comparison of two vectors. Each vector has a magnitude and a phase, both of which vary with time, and each contains a small amount of random noise. The amplitude at a given frequency will vary slowly across blocks for a given channel, indicating highly correlated blocks. The phase angle variation across blocks changes (rotational orientation) rapidly compared with the amplitude variation, indicating a lower degree of correlation between blocks. Thus, if one is interested in estimating the phase angle difference (i.e., calculating a spatial correlation matrix) between channels in an array and the signal duration is fixed, it is advantageous to use a large number of highly overlapped blocks (compare Fig. 36 and Fig. 38).

Continuing with the same data, we contrast the previous four satisfactory wavenumber spectra with another pair of 11-Hz ML wavenumber estimates formed using a single block of 512 points. This is theoretically more than twice the signal duration needed to adequately observe an 11-Hz waveform propagating at 220 m s^{-1}.

The 11-Hz ML wavenumber spectrum in Figure 40 applied a Blackman window taper to the block of data, and the 11-Hz ML wavenumber spectrum in Figure 41 used a boxcar window function. Figure 40 has an acceptably peaked spectral maximum indicating a source direction of 258° and a phase velocity of 219 m s^{-1}. However, this estimate has a considerably higher background energy level (–18 dB) compared with the previous examples. The highest spectral side lobe has an energy level of –12 dB. In a rather dramatic contrast, we note that the ML wavenumber spectrum

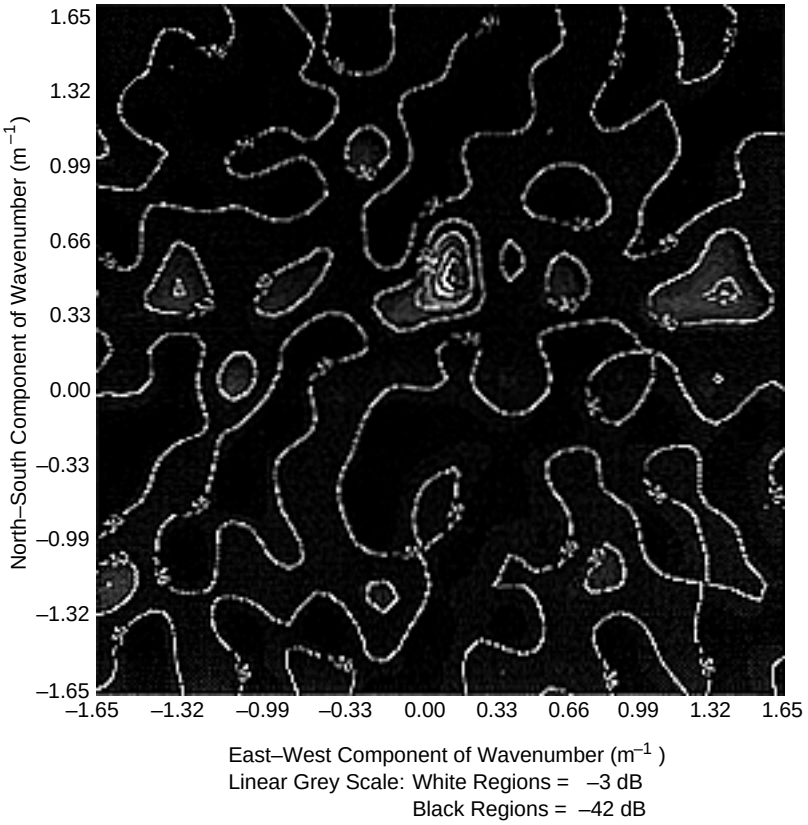

Figure 38. ML wavenumber estimate at 11 Hz for waveforms shown in Figure 35: Blackman taper, three blocks (at 53% overlap), segment length = 1024; produces a source direction of 258° with a velocity of 219 m s–1.

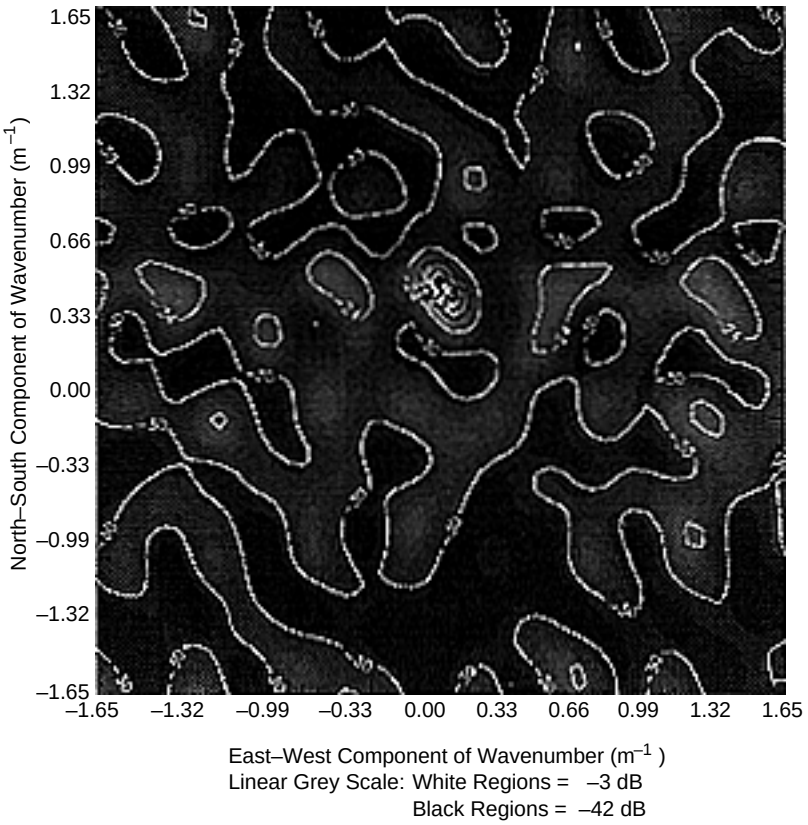

Figure 39. ML wavenumber estimate at 11 Hz for waveforms shown in Figure 35: boxcar taper, three blocks (at 53% overlap), segment length = 1024; produces a source direction of 255° with a velocity of 271 m s–1.

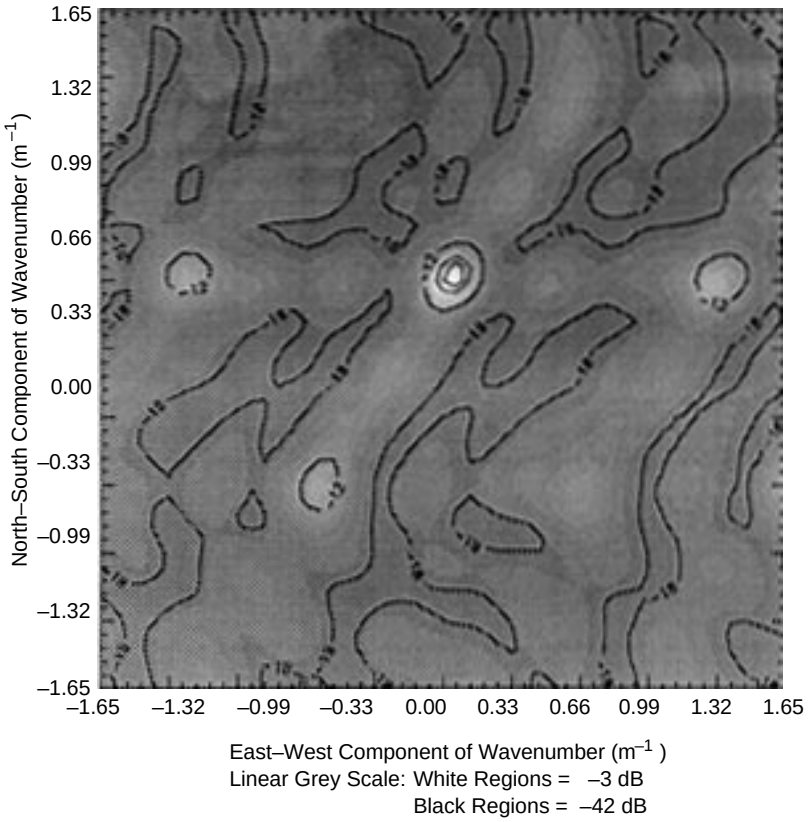

Figure 40. ML wavenumber estimate at 11 Hz for waveforms shown in Figure 35: Blackman taper, one block, segment length = 512. Spectra give a source direction of 25° and velocity of 219 m s–1.

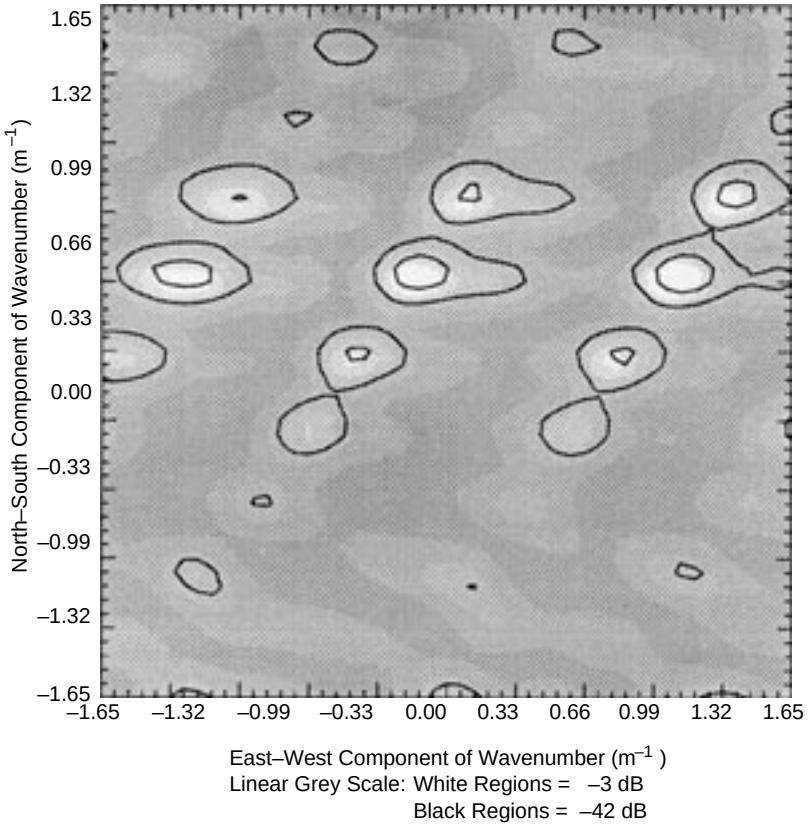

Figure 41. ML wavenumber estimate at 11 Hz for waveforms shown in Figure 35: boxcar taper, one block, segment length = 512. Beam is unfocused.

in Figure 41 is essentially unfocused for the boxcar taper.

Figure 41 is an extreme example of beamformer failure; however, it was not uncommon to encounter similar problems in less coherent frequency bins with more reasonable OBAFFT parameters. The failure of the beamformer to focus is most likely due to the highly biased nature of the frequency-domain phase angle caused by energy leakage from neighboring frequency bins. Such bias effects are particularly problematic with the boxcar window. The above examples show the extent to which the introduction of a high degree of bias and variance in the frequency domain estimate impacts the wave number estimate.

Considering the wavenumber results in this section and those given in other sections, we make several generalizations concerning the impact of the OBAFFT parameters on ML beamformer. In virtually all the examples discussed, the application of a strongly tapered, low-resolution, low-bias, time-domain window function (such as the Blackman taper) produced a higher resolution wavenumber estimate with lower background energy levels when compared with wavenumber estimates using high-resolution, high-bias, time-domain tapers (such as the boxcar function).

Specifying large numbers of blocks in the OBAFFT estimation of the spatial correlation matrix mitigated the impact of the high-bias window functions. Improvements in beamformer performance were observed even when blocks were overlapped by as much as 95%. The unexpected benefit of using highly overlapped blocks in the estimate of the spatial correlation matrix may be explained by noting that the phase angle for a given frequency bin in each block varies rapidly between blocks and therefore has a much smaller degree of correlation between blocks as compared with power spectra estimates. The variance analysis was helpful in partially explaining the beamformer's dependence on the OBAFFT parameters. A more complete explanation will have to consider the phase angle bias effects as well.

6. CONCLUSIONS

Capon's minimum variance (maximum likelihood) beamformer produces reliable direction estimates for a U.S. Army M60 tank moving at 4.5 m s^{-1} using an array of vertical-component geophone signals. Accurate direction estimates were obtained at ranges from 50 to 500 m from the array origin. The vertical-geophone responses to the M60 tank were dominated by the presence of Rayleigh surface wave energy with spectral peaks at 11 and 30 Hz and a propagation velocity of 220 m s^{-1}. Most wavenumber estimates used the highly coherent secondary maxima in the vicinity of the 11-Hz frequency bins. It was difficult to obtain reliable wavenumber estimates in the vicinity of the 30-Hz spectral maxima. It is hypothesized that the low coherence in the vicinity of 30 Hz is due to interference at the sensor between acoustic and seismic waves.

Maximum-likelihood wavenumber estimates of .45 caliber blank pistol shots exhibited two distinct propagation modes. The first wave phase arrives with a propagation velocity of 338 m s^{-1} and is interpreted as an acoustic excitation of the ground in the vicinity of the geophone. The second wave phase arrives with a propagation velocity of approximately 220 m s^{-1} and is interpreted as a Rayleigh surface wave that is excited by acoustic-to-seismic coupling near the source. Wavenumber estimates of vertically delivered sledgehammer blows also exhibited surface wave propagation modes that had the same phase velocity.

In general, direction and velocity estimates obtained from wavenumber spectra showed good agreement with known source positions and velocity estimates produced by time-domain moveout analyses. However, it was observed that changes in the parameters used to estimate the spatial correlation matrix could produce wavenumber bias effects. These spatial frequency bias effects were strongly dependent on the type of window taper applied to the time series data and the number of blocks used in the estimate of the spatial correlation matrix. It was observed that low-resolution, low-bias window types produced the highest resolution wavenumber spectra with the least wavenumber bias and highest signal-to-noise ratios. Utilizing large numbers of blocks in the estimate of spatial correlation matrix mitigated the impact of window taper choice. In some cases improvements were found in the wave-number spectra even when block overlaps were as high as 95%.

LITERATURE CITED

Albert, D.G. (1989) Preliminary analysis of acoustic-to-seismic coupling experiments at Grayling, Michigan. Paper presented at the 17th Meeting of NATORSG.11, 23–27 May 1988, Issy-les-

Moulineaux, France. USA CRREL Internal Report 1027.

Capon, J. (1969) High-resolution frequency–wavenumber spectrum analysis. *Proceedings of the IEEE*, **57**: 1408–1418.

Capon, J., R.J. Greenfield and R.J. Kolker (1967) Multidimensional maximum-likelihood processing of a large aperture seismic array. *Proceedings of the IEEE*, **55**(2): 192–211.

Carter, G.C. (1977) Bias in bearing estimation resulting from source motion. *Journal of the Acoustical Society of America*, **62**(6): 1447–1448.

Cress, D.H. (1976) Seismic methods of locating military ground targets. U.S. Army Waterways Experiment Station, Vicksburg, Mississippi, Paper M-76-13.

De Graaf, S.R. and D.H. Johnson (1985) Capability of array processing algorithms to estimate source bearings. *IEEE Transactions*, Acoustics, Speech, and Signal Processing, **ASSP-33**(6): 1368–1379.

Farrland, W.R. and D.L. Bell (1982) Quaternary Geology of Southern Michigan, 1:500,000.

Gragg, R.F. (1990) Correlations among the modal components of the far field of a moving source: Low-frequency Doppler effects in shallow water. *Journal of the Acoustical Society of America*, **88**(5): 2326–2337.

Hahn, W.R. (1975) Optimum signal processing for passive sonar range and bearing estimation. *Journal of the Acoustical Society of America*, **58**: 201–207.

Harris, F.J. (1978) On the use of windows for harmonic analysis with the discrete Fourier transform. *Proceedings of the IEEE*, January, **66**: 51–83.

Johnson, D.H. (1982) The application of spectral estimation methods to bearing estimation problems. *Proceedings of the IEEE*, September, **70**(9): 1018–1028.

Kelley, E.J. (1967) Response of seismic arrays to wideband signals. Massachusetts Institute of Technology, Lincoln Laboratory, Technical Note 1967-30, June.

Knapp, C.H. and G.C. Carter (1977) Estimation of time delay in the presence of source or receiver motion. *Journal of the Acoustical Society of America*, **61**(6): 1545–1549.

Lacoss, R.T., R.K. Brienzo and T.E. Jones (1991) Characteristics of acoustic and seismic signals for vehicle detection and direction finding. Paper presented at the 24th Meeting of the NATO AC/243, Panel 3, Research Study Group 11, Los Angeles, California.

Lilienthal, R.T. (1978) Stratigraphic cross-sections of the Michigan Basin (Geological Survey Division, Lansing, Michigan). Report of Investigation 19.

Moran, M.L. (1991) Users manual for ESTK2D.FOR and ESTK1D.FOR wavenumber estimation routines. USA Cold Regions Research and Engineering Laboratory, Special Report 91-15.

Nawab, H. S., F.U. Dowla and R.T. Lacoss (1985) Direction determination of wideband signals. *IEEE Transactions*, Acoustics, Speech, and Signal Processing, **ASSP-33**(4): 114–122.

Priestly, M.B. (1981) *Spectral Analysis and Time Series*. New York: Academic Press.

Welch, P.D. (1967) The use of fast Fourier transform for the estimation of power spectra; a method based on time averaging over short, modified periodograms. *IEEE Transactions*, Audio and Electroacoustics, **AU-15**: 70–73.

REPORT DOCUMENTATION PAGE

Form Approved
OMB No. 0704-0188

1. AGENCY USE ONLY (Leave blank)	2. REPORT DATE	3. REPORT TYPE AND DATES COVERED
	June 1996	

4. TITLE AND SUBTITLE
Source Location and Tracking Capability of a Small Seismic Array

5. FUNDING NUMBERS
DA: 4A762784AT42
TA: SS
WU: E02

6. AUTHORS
Mark L. Moran and Donald G. Albert

7. PERFORMING ORGANIZATION NAME(S) AND ADDRESS(ES)
U.S. Army Cold Regions Research and Engineering Laboratory
72 Lyme Road
Hanover, N.H. 03755-1290

8. PERFORMING ORGANIZATION REPORT NUMBER
CRREL Report 96-8

9. SPONSORING/MONITORING AGENCY NAME(S) AND ADDRESS(ES)

10. SPONSORING/MONITORING AGENCY REPORT NUMBER

11. SUPPLEMENTARY NOTES

12a. DISTRIBUTION/AVAILABILITY STATEMENT
Approved for public release; distribution is unlimited.

Available from NTIS, Springfield, Virginia 22161.

12b. DISTRIBUTION CODE

13. ABSTRACT (*Maximum 200 words*)

Recordings of seismic wavefields from various sources were obtained using a small array of vertical-component geophones under winter conditions at Grayling, Michigan. These data were processed using a frequency-wavenumber domain Capon minimum variance beamformer to estimate the bearing angle and propagation velocity of the waves emitted from the source. The cross power matrix was adaptively estimated using a tapered block-averaging procedure. The wave sources were sledgehammer blows on the ground surface, .45 caliber blank pistol shots, and an M60 tank moving at 4.5 m s^{-1} along a road near the array. Reliable wavenumber spectra were obtained for all sources. Processing results for the hammer blows show that the dominant seismic arrival is a Rayleigh wave traveling at roughly 220 m s^{-1}. For the pistol shots, two arrivals corresponding to the airwave (338 m s^{-1}) and the air-coupled Rayleigh waves (220 m s^{-1}) were observed. The results for these sources were relatively insensitive to the processing parameters used. For the moving vehicle, the dominant signals observed were Rayleigh waves (220 m s^{-1}). Accurate locations were obtained for this moving source, although the processing parameters had to be carefully selected, and the choice of frequency parameters affected the accuracy of the wavenumber results. Maximizing the number of degrees of freedom and the coherence of the frequency estimates and minimizing the variation of the coherence across adjacent frequency bins provided the most consistently reliable strategy for obtaining accurate wavenumber estimates for the moving vehicle. The sensitivity of the wavenumber estimates to the frequency processing parameters seems to be related to the bias in the phase spectra of the signals and will potentially occur in any bearing estimation method that uses temporal frequncy phase spectra.

14. SUBJECT TERMS			15. NUMBER OF PAGES
	Beam forming	Seismic array processing	44
	Capon method	Target location and tracking	16. PRICE CODE
	Frequency-wavenumber estimation	Unattended ground sensors	
	Maximum likelihood method	Wavenumber bias effects	

17. SECURITY CLASSIFICATION OF REPORT	18. SECURITY CLASSIFICATION OF THIS PAGE	19. SECURITY CLASSIFICATION OF ABSTRACT	20. LIMITATION OF ABSTRACT
UNCLASSIFIED	UNCLASSIFIED	UNCLASSIFIED	UL